Multiscale analysis of thermomechanical stresses in double wall transpiration cooling systems for gas turbine blades

Christos Skamniotis, Matthew Courtis, Alan C.F. Cocks

Department of Engineering Science, University of Oxford, Parks Road,

Oxford OX7 6DP, UK

ABSTRACT

Double wall transpiration cooling (DWTC) is a new technology that allows the gas turbine inlet temperatures to be increased beyond current levels to promote higher engine efficiency. DWTC systems consist of outer hot and inner cooler walls, connected by pedestals, which contain film cooling and impingement holes, respectively. In order to employ these new systems, an evaluation of the stresses that drive fatigue and ratchetting at critical stress raisers is essential. We present a modelling framework which combines Computational Fluid Dynamics (CFD)-heat transfer solutions for the temperature field in DWTC systems, with theoretical and Finite Element (FE) elastic solutions for the thermal (T) stress and centrifugal (CF) stress fields. We demonstrate that uniaxial tensile CF loading causes much higher stress concentration factors (SCF) at cooling holes and wall-connecting pedestals than the thermally induced biaxial stresses. A theoretical framework is developed, supported by FE studies, that captures the dependence of the SCF on important geometric parameters, such as wall thicknesses, pedestal height and hole size, spacing and inclination angle, which provides important information for the optimisation of these systems. A key observation of relevance to both conventional and non-conventional turbine blade designs, is that the superposition of tensile CF stresses to compressive T stresses is beneficial for the performance at the critical film hole features; for double wall blades, however, the superposition degrades the performance at impingement holes and pedestals, as in these locations the T stresses

are also tensile. These stresses can be balanced by using an optimal wall thickness ratio. Our elastic solutions can be readily used in analyses for predicting structural ratchet boundaries based on shakedown theory and the local cyclic strain range that drives thermomechanical fatigue in DWTC systems.

Keywords: cooling holes, low cycle fatigue, thermal stresses, centrifugal stresses, stress concentration.

Nomenclature

Abbreviations

DWTC = double wall transpiration cooling

TIT = turbine inlet temperature

LCF = low cycle fatigue

FE = Finite elements

CFD = computational fluid dynamics

ICC = internal convective cooling

T = thermal loading/stress

CF = centrifugal loading/stress

2D = two-dimensional

3D = three-dimensional

SCF = stress concentration factor

MPC = multipoint constraint ABAQUS subroutine

UDISP = user defined displacement ABAQUS subroutine

Symbols

Thermal

h_∞ = external heat flux (W/m²)

η_f = film cooling effectiveness

α_t = turbulent thermal diffusivity (m^2/s)

ξ_{decay} = characteristic film decay length (m)

T_∞ = hot gas mainstream flow temperature (°C)

$T_{coolant}$ = coolant temperature entering the impingement hole (°C)

T_{max} = maximum temperature at outer hot wall surface (°C)

T_{med_h} = temperature at inner hot wall surface (°C)

T_{med_c} = temperature at inner cool wall surface (°C)

T_{min} = minimum temperature at outer cool wall surface (°C)

T_0 = room temperature (°C)

ΔT = thermal difference (°C)

Structural

L = component length (mm)

R_{tip} = blade tip radius with respect to axis of rotation (mm)

t = wall thickness (mm)

A = cross-sectional area (mm^2)

V = volume (mm^3)

H = pedestal height/wall spacing (mm)

H_c = distance between wall mid-planes (mm)

R = radius of geometric curvature (mm)

S = pedestal spacing (mm)

Z = pedestal centreline distance (mm)

D = diameter (mm)

ρ = fillet radius (mm)

γ = film hole inclination (°)

Material

E = Elastic Modulus (MPa)

ν = Poisson's ratio

ρ = density (tn/mm³)

a = thermal expansion coefficient (1/°C)

k = thermal conductivity (W/m·°C)

Mechanical

$\mathbb{M}$ = blowing ratio

v_∞= hot gas mainstream flow velocity (m/s)

v_{film} = coolant exit velocity at film hole (m/s)

$\dot{m}_{coolant}$ = coolant mass flow rate (kg/s)

ω = angular velocity (rad/sec)

dm = infinitesimal mass (tn)

$p_{s,outlet}$ = external pressure used in aerothermal CFD analysis (MPa)

p = gas pressure in turbine blade used in stress analysis (MPa)

F = external force (N)

$\mathcal{N}$ = internal membrane force (N)

N = internal membrane force per unit length (N/mm)

M = internal bending moment per unit length (N·mm/mm)

κ = bending curvature (mm^{-1})

I = second moment of area (mm^4)

ε = strain

σ = uniaxial (Cauchy) stress or maximum absolute principal stress (MPa)

σ_j = stress component (MPa) in j direction (MPa)

σ_1 = maximum principal stress (MPa)

σ_2 = medium principal stress (MPa)

σ_3 = minimum principal stress (MPa)

Accents

$\bar{}$ = normalised quantity

Subscripts

$hwall$ = outer (hot) layer property

$cwall$ = inner (cooler) layer property

ped = pedestal property

ξ = streamwise direction

ζ = spanwise direction

y = position through wall thickness (mm)

θ = circumferential axis/direction

z = longitudinal axis/direction

r = radial axis/direction

x = x direction

y = y direction

z = z direction

1. Introduction

Increasing the gas turbine inlet temperature (TIT) beyond current values promises substantial efficiency benefits in jet engine and power plant applications [3], thus addressing the timely need for lower carbon dioxide emissions [4] and lower travel costs. Compared to the advances arising from thermal barrier coatings, metal alloys and manufacturing, the evolution of cooling technologies so far has marked the most important impact on the continuously increasing TIT over the last 60 years [5, 6].

Double wall transpiration cooling (DWTC) is a new system that promises to continue the increase of TIT in engines by reducing the heat flux into metallic components more effectively than current systems [7]. Its implementation in high pressure gas turbine blades is of great importance, because the fuel efficiency and specific power output of engines rely heavily on the temperatures that these components can withstand [5]. An idealised DWTC system is depicted in Fig 1a, along with its periodically repeating unit cell in Fig 1b. The outstanding cooling effectiveness and convective efficiency of DWTC owes to the synergy of [8, 9]:

- external film cooling through inclined holes in the outer hot wall of the component,
- internal impingement cooling by the use of impingement holes in an inner cool wall,
- heat conduction from the hot wall to the cool wall through the connecting pedestals.

Key challenges for incorporating DWTC into real engines is: the maintenance of adequate coolant flow with minimum turbine stage efficiency losses [10]; the production of the required film distribution with minimum mixing with the mainstream flow [11]; the manufacturing of intricate architectures [11, 12]; and the design against creep-fatigue failure [13].

Although the research relating directly to these is very recent, a wealth of relevant literature is available, particularly concerning the general concept of film cooling [11, 14]. This literature has mainly dealt with either the aerothermal aspects of film cooling related to the flow of fluids around film holes to determine surface temperatures and heat conduction coefficients or mechanical aspects related to deformation and damage development, particularly around the film holes. Aerothermal studies have taken into account coolant-mainstream gas interactions [15, 16], turbulence and vorticity production [17, 18], crossflow orientation effects [19], and the effect of hole shape, spacing [19-21] and surface roughness [22]. The evaluation of mechanical performance general centres on prediction of damage development and failure under creep-fatigue conditions [23-26] informed by based on thermal-elastic stress analysis [27] and informed by thermomechanical fatigue and creep rupture experiments [25, 26, 28, 29]. More recently, crystal plasticity Finite Element (FE) modelling

approaches have been employed [23, 30] which take into account the effect of crystallographic orientation on deformation and damage [24].

Recent studies of DWTC systems, have built on this body of research. Murray et al [2] have developed an decoupled conjugate method which provides the film cooling effectiveness distribution and the steady state temperature field through studies of representative DWTC geometries. The efficiency of the computational method arises from the fact that only the internal coolant flow is simulated using Computational Fluid Dynamics (CFD), with empirical correlations and film superposition used to compensate for the external cooling. Murray et al [7] have also developed a new experimental facility that reproduces closely the Re and Biot numbers seen during engine conditions and uses infrared thermography to measure cooling effectiveness; the results agreed with those predicted by the decoupled conjugate method [2]. Ngetich et al [31] utilised the same conjugate method to determine the transpiration cooling performance of a large scale double wall turbine blade model in terms of a two-dimensional film cooling effectiveness distribution. The merit of the approach is that it allows for a rapid evaluation of the film effectiveness and blade external temperature distributions as well as of the coolant mass flow consumption. Elmukashfi et al [32] explored the thermoelastic stress field in simple double wall elements, including the effect of cooling parameters, i.e. Re and Biot number, and perturbations of the temperature field, on peak stresses.

In contrast to the aerothermal aspects of DWTC, systematic studies of the mechanical performance is limited to a few recent studies [12, 32-34], mainly conducted by the authors. These studies indicate that DWTC systems can experience severe thermal stresses [34] as significant stress concentration factors (SCF) occur at holes and pedestals [12]. Values of SCF ≈ 4 at the acute wedge (Fig 1b) of inclined film holes have been shown to cause severe local cyclic plasticity and low cycle fatigue failure (LCF) [13]. This phenomenon is enhanced by the sharp reduction in yield strength of nickel alloys at temperatures $T > 800$ ºC [35]. It was suggested in [13] that LCF is not an issue for internal stress raisers i.e. the inner pedestal-wall fillets and impingement holes (see Fig 1b), as these

experience temperatures $T < 800$ °C. It was therefore concluded that LCF at film holes is the most important failure process [13] and that performance can be optimised via local geometric changes, i.e. by altering the hole inclination-shape-size to reduce the SCF [12], and through global changes, i.e. reducing the cool wall thickness to lower the nominal compressive stresses at the film hole [13], at the cost of increasing tensile stresses at internal features. Those recommendations, however, should be interpreted with caution due to the following reasons:

- In [34] it was assumed that a thermal gradient develops only across the outer hot wall. The thermal gradient which in practise occurs across the pedestal [7], will enhance the wall temperature mismatch, increasing the thermal stresses in both walls. Reducing the cool wall thickness could then overly increase the stress at internal features.
- Centrifugal (CF) loading has been ignored so far [12, 32-34], despite its significance in turbine blades [36]. Since CF loading is generally tensile, the thermally (T) induced compressive film hole stresses can eventually reduce and the tensile stresses at internal features may increase.

The above trade-off that can arise under combined T-CF loading is analysed here by superposing CF T stresses for a range of geometric and T-CF loading combinations. Both full-scale double wall blade geometries and repeating models extracted from these geometries are considered; this will allow us to answer the following questions.

1. How are T stresses influenced by first and high order variations of the temperature field in realistic DWTC systems?
2. How severe are CF stresses compared to T stresses in high pressure double wall blades?
3. How does the presence of pedestals and holes influence CF stresses?
4. What load-displacement boundary conditions should be used when analysing a repeating block of a double wall blade?
5. What are the options for optimising a DWTC blade for a particular T-CF loading condition.

This paper is the first to analyse combined thermal and centrifugal stresses in double wall geometries using realistic temperature distributions, based on those determined using the decoupled conjugate method of Murray et al [2]. We limit our consideration to isotropic elastic material behaviour. This allows us to develop analytical and FE solutions that provide information about how stresses change when key geometric parameters and details of the temperature field and centrifugal loading are changed. This type of information is important for the design of new DWTC systems, where geometries and operating conditions often need to be simultaneously optimised. A key consideration in design is the creep-fatigue performance of the system, which requires an understanding of the cyclic plastic and creep response of the material. Despite these features of the material response missing from the calculations presented here, strategies have been established for incorporating these effects into structural integrity assessments which employ elastic calculations of the type described here as a major input [13, 37]. Thus, the elastic calculations presented here provide an important stepping-stone to evaluating performance and optimising blade design. We recognise that for single crystal blades, anisotropy and crystallographic effects can be important. To date, this has only been explored for conventional single wall blades without holes, with the main focus on crystallographic orientation effects [38] and creep-fatigue driven crystallographic slip mechanisms [39-42], while also taking into account the transient thermomechanical loading response [43-45]. The aim of the approach and simplifications adopted here is to provide important physical insights into the response of these new double wall systems and in the process answer questions 1-5 above. The benefits and implications of these idealisation are discussed in Section 6.

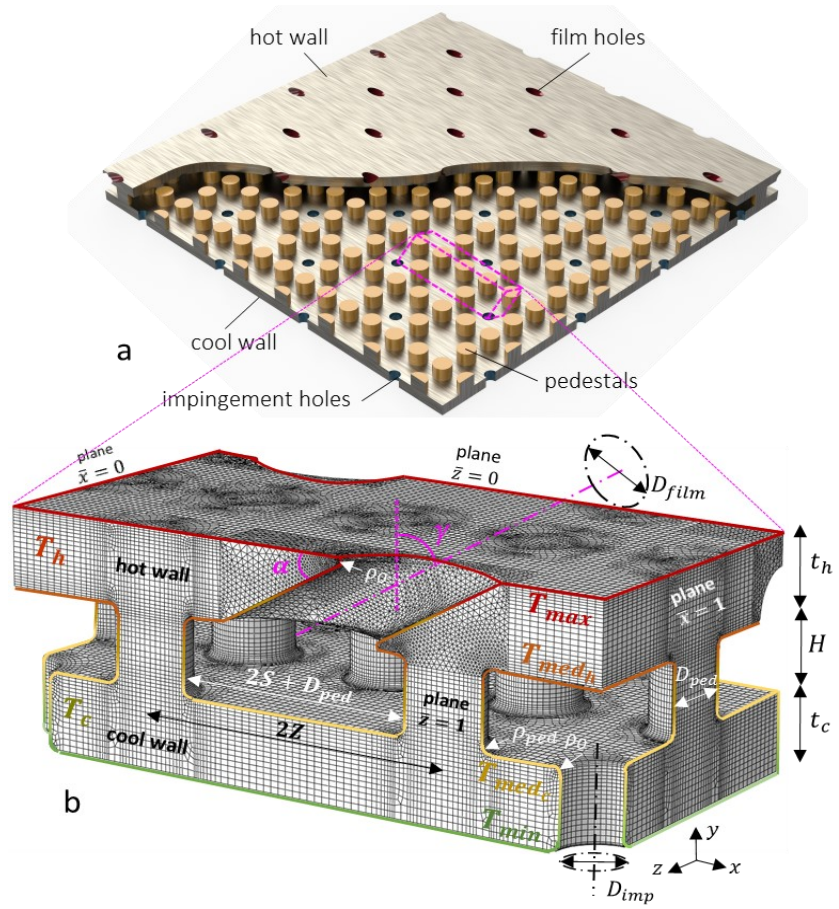

Figure 1. (a) A double wall transpiration cooling (DWTC) system adapted from [2]; cooling features are indicated. (b) Repeating unit cell and mesh used in FE analysis, with idealised temperature field and dimensions denoted.

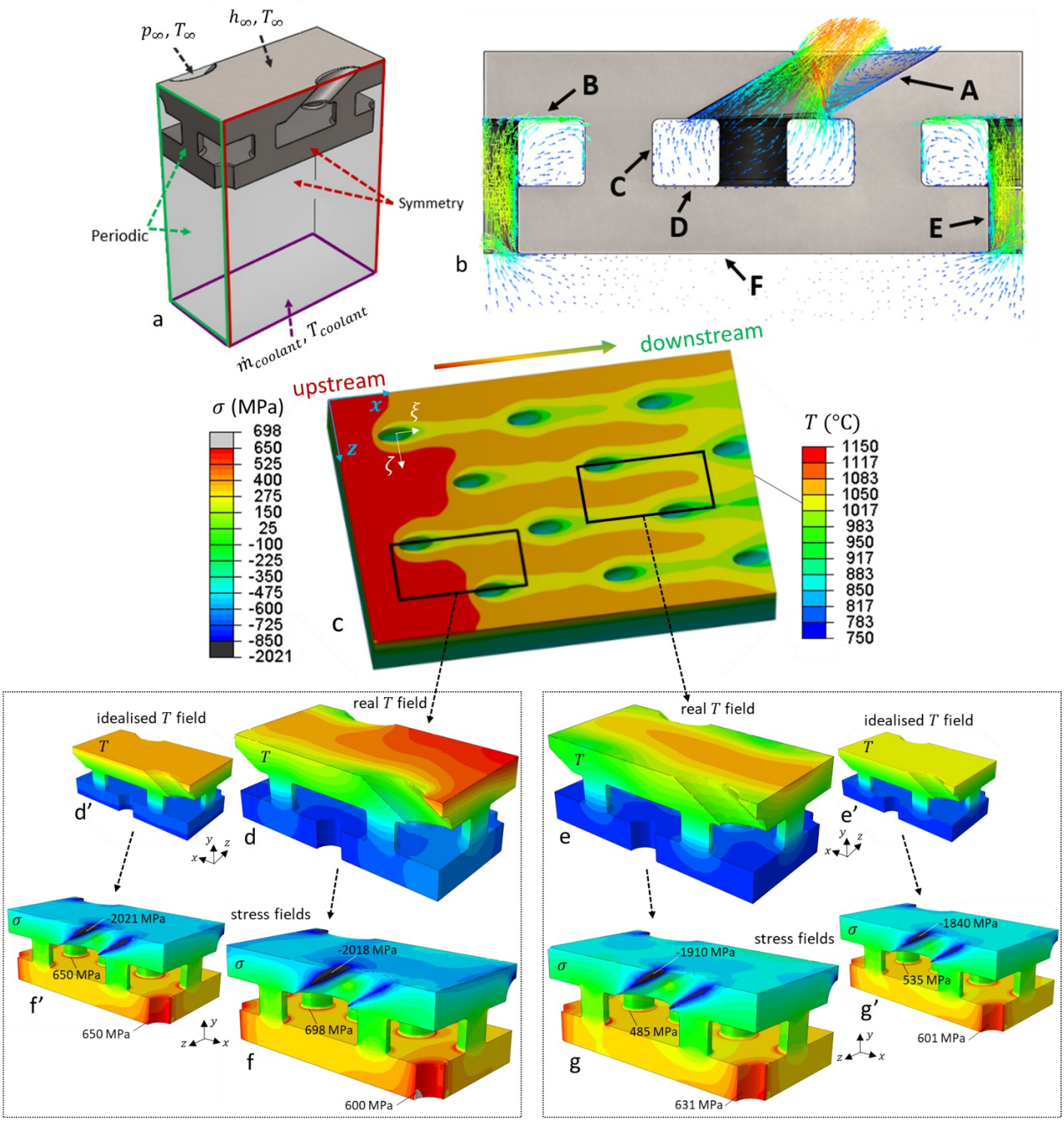

Figure 2. (a) CFD model used for aerothermal analysis of the system in Fig 1, with boundary conditions denoted. (b) Coolant flow migration patterns at a symmetry plane; regions of convective cooling are indicated from A to F. (c) Steady state temperature field obtained from the aerothermal analysis; two characteristic repeating unit cells corresponding to the upstream and downstream regions used in thermal stress analysis are indicated. (d-e) Real temperature fields for the two characteristic unit cells. (e'-d') Idealised temperature fields in the unit cells in (d-e). (f-g)-(f'-g') Maximum absolute principal stress, $\sigma = max\langle|\sigma_1|, |\sigma_2|, |\sigma_3|\rangle$, fields corresponding to the temperature fields of (d-e)-(d'-e').

Table 1. Parameters used in the study.

Material		Structural		Aerothermal CFD analysis		Thermal loading		Centrifugal loading	
E	100 GPa	$t_h, t_c, H, S,$ $D_{ped}, D_{film},$ D_{imp}	1 mm	T_∞	1597 °C	T_{max}	1038 °C	ω	858.5 rad/s
ν	0.4	Z	2 mm	v_∞	270 m/s	T_{med_h}	940 °C	R_{tip}	400 mm
a	$17.4{\cdot}10^{-6}$ 1/°C	ρ_{ped}, ρ_O	0.1 mm	p_∞	3.4 MPa	T_{med_c}	784 °C	L	60 mm
k	19.4 W/m°C	ρ_b	3 mm	h_∞	772 W/m^2	T_{min}	772 °C	L_x	45 mm
ρ	8.7 tn/mm^3	γ	60°	$T_{coolant}$	727 °C	ΔT	266 °C	$\tilde{L}_x$	16988 mm
				$\dot{m}_{coolant}$	$3{\cdot}10^{-4}$ kg/s	$\overline{\Delta T}_{hwall}$	0.37		
						$\overline{\Delta T}_{ped}$	0.58		
						$\overline{\Delta T}_{cwall}$	0.045		

Table 2. Contribution of each geometric feature of Fig 2b to the total internal convection cooling.

	Feature	%
A	film holes	14
B	inner hot wall surface	51
C	pedestals	22
D	inner cool wall surface	4
E	impingement holes	3
F	outer cool wall surface	6

2. Temperature and thermal stress fields

2.1 Outline

In this section we determine the aerothermal response of the DWTC system of Fig 1a, along with the associated steady state temperature field. The temperature field is then idealised and used in an FE thermal stress analysis to identify the features that dictate critical thermal stresses.

2.2 Aerothermal calculations

To determine the steady state temperature field shown in Fig 2c we employ the decoupled conjugate technique developed by Murray et al. [10], which consists of three major steps:

1) a computational Fluid Dynamics (CFD) simulation using the repeating block model in Fig 2a,
2) the processing of CFD results through empirical correlations proposed by Goldstein [46] and Sellers [47],
3) the determination of boundary conditions for performing an FE heat transfer simulation.

The details of each step are provided in Appendix A. Geometric dimensions for the CFD model of Fig 2a are given in Fig 1b and tabulated in Table 1, along with the boundary values used in the simulations. Fig 2b shows the steady state coolant velocity vectors at the symmetry plane and Table 2 shows the percentage contribution of each feature to the total internal convective cooling (ICC).

A small fraction of ICC is observed (Table 2) to occur along the impingement hole and outer cool wall surfaces (respectively denoted as E and F in Fig 2b). The impingement jet travels across the inner cavity and stagnates on the inner surface of the outer hot wall (denoted as B in Fig 2b); the flow is then directed radially in the form of lateral jets parallel to the wall surface. The latter contributes 51% of the total ICC (Table 2). The lateral jets are obstructed by the pedestals (denoted as C in Fig 2c) and they migrate towards the film holes. The film holes contribute both to the total ICC (14 % - Table 2) and to the reduction of the external heat flux, as evidenced in Fig 2c by the reduced external metal temperatures adjacent to the film holes and the overall reduction of temperature from the upstream to the downstream region of the domain.

2.3 Temperature field idealisation

We consider the temperature fields shown in Figs 2d-e for unit cells of the upstream and downstream regions of the array (see Fig 2c). The cool wall essentially experiences a constant temperature, whereas thermal gradients exist along the pedestals and across the hot wall. These are classified as 1st order features of the temperature field. The thermal gradient varies with in-plane position, since the film effectiveness decreases with distance from the film holes. This is classified as a 2nd order feature of the temperature field and it becomes more pronounced for the unit cell of the

upstream region in Fig 2d where there is no coolant film superposition. Film superposition gives rise to a 3rd order feature in that the average temperature in a unit cell decreases along the downstream direction (Figs 2d-e).

FE thermal stress analysis is performed not only for the 'real' temperature fields in Figs 2d-e, but also for the corresponding idealised temperature fields shown in Figs 2d'-e'; these are the fields that occur by applying the computed average temperature uniformly over each of the four wall surfaces in Figs 2d-e. These temperatures are $T_{max} = 1071$ °C, $T_{med_h} = 954$ °C, $T_{med_c} = 790$ °C, $T_{min} = 780$ °C (denoted in Fig 1b) for Fig 2d and $T_{max} = 1038$ °C, $T_{med_h} = 940$ °C, $T_{med_c} = 784$ °C, $T_{min} = 772$ °C for Fig 2e. These give the average thermal differences, $\Delta T_{hwall} = T_{max} - T_{med_h}$, $\Delta T_{ped} = T_{med_h} - T_{med_c}$ and $\Delta T_{cwall} = T_{med_c} - T_{min}$ across the hot wall, the pedestal and the cool wall, respectively (see Fig 3a); note that ΔT_{cwall} is negligible in both Figs 2d-e.

2.4 Thermal stress field calculations

The details of the FE thermal stress analysis are given in Appendix B, the material model parameters are given in Table 1 and the results (maximum absolute principal stresses, $\sigma = \max\langle|\sigma_1|, |\sigma_2|, |\sigma_3|\rangle$ are shown in Figs 2f-g, f'-g'. A common feature in these figures is that the cool wall effectively experiences pure tension, the hot wall undergoes combined compression and bending, and the critical stress locations are the outer acute wedge-vertex of the film hole (peak compressive stress), the impingement hole (peak tensile stress) and the inner pedestal fillets. The above thee critical stresses do not change significantly between the real and the idealised temperature profiles, not only for the unit cell of the downstream region (compare Fig 2g with Fig 2g′) but also for the unit cell of the upstream region (compare Fig 2f with Fig 2f′). This suggests that peak stresses are dictated by the 1st order features of the temperature field and that the 2nd order features are much less significant. This is consistent with the study by Elmukashfi et al [32] on simple double wall geometries without features.

A second observation is that peak stresses are generally higher in the upstream region (Figs 2f-f') compared to the downstream region (Figs 2g-g′). This is explained by the fact that for Figs 2f-f' we compute an average global gradient, $\Delta T = \Delta T_{hwall} + \Delta T_{ped} + \Delta T_{cwall} = 291$ °C, in which the contribution of the thermal difference through the hot wall is $\overline{\Delta T}_{hwall} = \Delta T_{hwall}/\Delta T = 0.4$, whereas in Figs 2g-g′ $\Delta T = 266$ °C and $\overline{\Delta T}_{hwall} = 0.37$. This indicates that not only the average temperature in the system changes in the downstream direction, but also the thermal difference distributions in the system. To explore how these distributions influence stresses, throughout the rest of this study we will use fixed $T_{max} = 1038$ °C, $\Delta T = 266$ °C, $\overline{\Delta T}_{cwall} = 0.045$ and only vary the critical $\overline{\Delta T}_{ped}/\overline{\Delta T}_{hwall}$ ratio, i.e. the proportion of the temperature drop along the pedestal compared to that across the outer hot wall.

3. Loading of turbine blade

3.1 Outline

This section now applies the idealised temperature field in Fig 2e′ to the FE double wall blade model of Fig 3. This will allow us to assess the relevance of the results for the unit cell of Fig 2e′ to stresses experienced in the turbine blade. In addition to thermal loading, we also analyse separately the cases of centrifugal (CF) loading, rotary acceleration loading and gas pressure loading. We then assess the severity of each loading type in double wall blade systems. Details of the blade geometry construction and boundary conditions are given in Appendix C; the results (maximum absolute principal stresses, $\sigma = max\langle|\sigma_1|, |\sigma_2|, |\sigma_3|\rangle$) are summarised in Fig 4.

3.1 Turbine blade stresses

Thermal (T) loading generally leads to much higher stress magnitudes compared to CF and P loading, with P stresses being the least severe (compare Figs 4c,f,i). Rotary acceleration was found

to cause maximum stresses of only ~10 MPa (not shown) in the vicinity of the external blade root fillet of the leading ledge region, despite the extreme angular acceleration, $\dot{\omega} = 858.5$ rad/s^2 used. This is expected in the sense that in contrast to the tensile CF stresses which scale with ω^2, bending stresses due to rotary acceleration scale with $\dot{\omega}$, for which $\dot{\omega} << \omega^2$. The stress field observed at a cross-section cut at 1/4 of the blade wall length L under T loading (Figs 4c) agrees with the corresponding nominal stress field shown earlier for the unit cell (Fig 2g') in that the hot wall undergoes (biaxial) bending and membrane compression and the cool wall experiences pure (biaxial) tension.

Thermal stresses in the hot wall decrease near the leading and the trailing edges (see Figs 4a-c), since these regions are not coupled with the inner cool wall here. This result should be interpreted with caution, since here we have considered simplified thermal loading conditions based on prescribed constant temperatures on each wall surface. In practise, the temperature field is more complex [48] for three main reasons: a) the heat flux onto the metal inherently increases at the leading edge and trailing edge regions and decreases at the blade suction side [49]; b) the film cooling effectiveness varies with the streamwise position, ξ, in the blade due to the variation of external gas pressure (Fig 4k) and curvature of the external blade surface [31]; and c) the absence of an inner cool wall, and thus impingement cooling, at regions near the trailing edge. Ngetich et al [48] reported an increase in the external metal temperature (here referred as T_{max}) near the leading edge and trailing edge regions as a result of the above effects. Although, external metal temperatures as a function of ξ are available in [31] for double wall blades, there is currently no information on the variation of internal temperatures, e.g. the inner wall temperature, T_{cwall} (see Fig 3c). The difference between T_{max} and T_{cwall} plays a major role in determining the thermal stresses. This explains why we have chosen to use the idealised temperature field here for the scope of comparing T, CF and P stresses.

In contrast to T loading, under pure CF loading and pure P loading the stresses increase from zero at the blade tip to a maximum at the root (Figs 4d-e, 4g-h). CF loading causes only tensile stresses in

the walls (Fig 4f) which decrease in the cross-sectional regions away from the x axis (also reported in [44]), as in these regions the body forces are inclined to the cross-sectional x-y plane. The bending nature of P loading is evidenced by the compressive and tensile stresses at the suction and pressure sides of the blade, respectively (Figs 4g-i) and by the fact that these stresses are largely localised at the external blade root fillet. The latter experiences the highest stresses (upper/lower bounds for each contour bar in Figs 4a,d,g) for all the three loading types T, CF, P. Note, however, that conventional turbine blades have a variable wall thickness profile (taper), especially along the spanwise direction, z, such that the taper ratio, A_{tip}/A_{root}, of the cross-sectional area between the root and the tip regions lies within $1/3 < A_{tip}/A_{root} < 1/4$ [36]; the cross-sectional shape also varies with z. As a rule of thumb, the critical stresses at the external blade root fillet have been assumed to reduce to 2/3 of the stresses for a constant wall thickness [36]. Hence, incorporation of the A_{tip}/A_{root} ratio into the current double wall blade is expected to reduce the peak stresses in the external blade root fillet in Figs 4a-b, 4d-e and 4g-h, for all the three loading types. This implies that for the current double wall blade, where stresses due to P loading (P stresses) are already low, these stresses can be potentially eliminated by optimising the wall thickness profiles. A geometric twist of the blade cross-section about the z axis (specified in [1]) is also often used to mitigate P stresses (and CF stresses) [50].

Note, however, that the low P stresses in Figs 4g-i are specific to the wall thicknesses, t, rib thickness and wall spacing of 1 mm, and can increase for larger blade wall lengths, L [50, 51]. Here we are interested in the sensitivity with respect to t and therefore we obtain the solutions in Fig 5 for the case of cool wall (and rib) thickness reduced by half i.e. 0.5 mm and the extreme case of single wall blade. Evidently P stresses in Fig 5a increase noticeably compared to Fig 4i (1 mm wall thicknesses) with the increase being more significant for the single wall blade (Fig 5d compared with Fig 4i), where the flexural stiffness is reduced. Simulations for 1 mm wall thicknesses and a wall spacing of 1.5 mm (instead of the 1 mm used in Fig 4i) caused an increase of peak P stresses (not shown), since increasing the wall spacing/pedestal height (for fixed outer blade profile) reduces the

contribution of the inner wall to the flexural stiffness. In contrast to P stresses, CF stresses display a minor dependence upon the wall thicknesses. Thermal stresses are instead very sensitive to the wall thickness ratio, t_c/t_h (compare Fig 5c with Fig 5f and Fig 4c), in line with our previous studies [12, 33, 34].

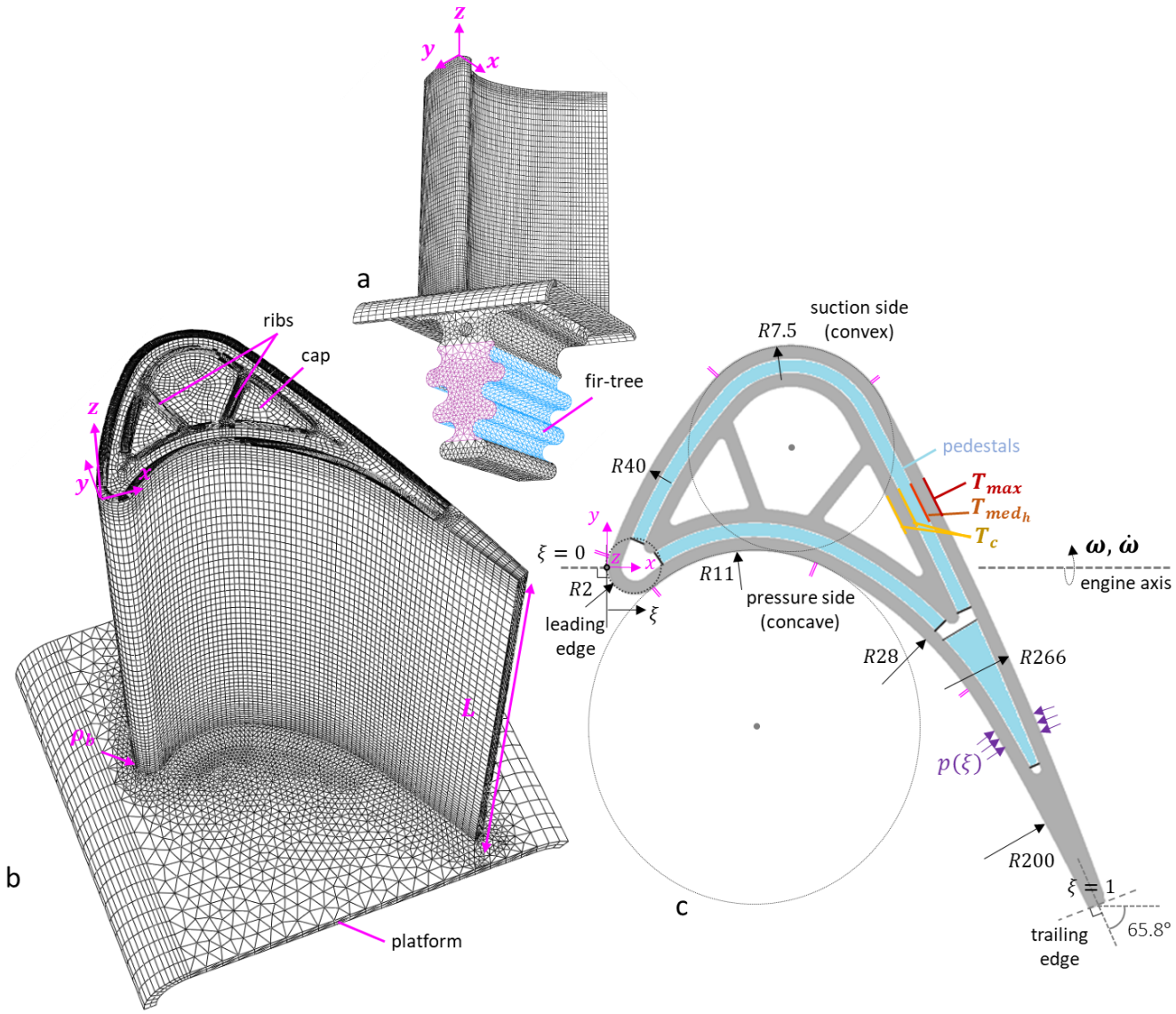

Figure 3. (a-b) FE double wall turbine blade model; external blade surface profile reproduced from [1]. (c) Blade cross section with local radii of curvatures, thermo-mechanical loading features and blade orientation with respect to the engine axis denoted; pink lines denote change in radius of curvature; blue regions represent the connection of walls with pedestals.

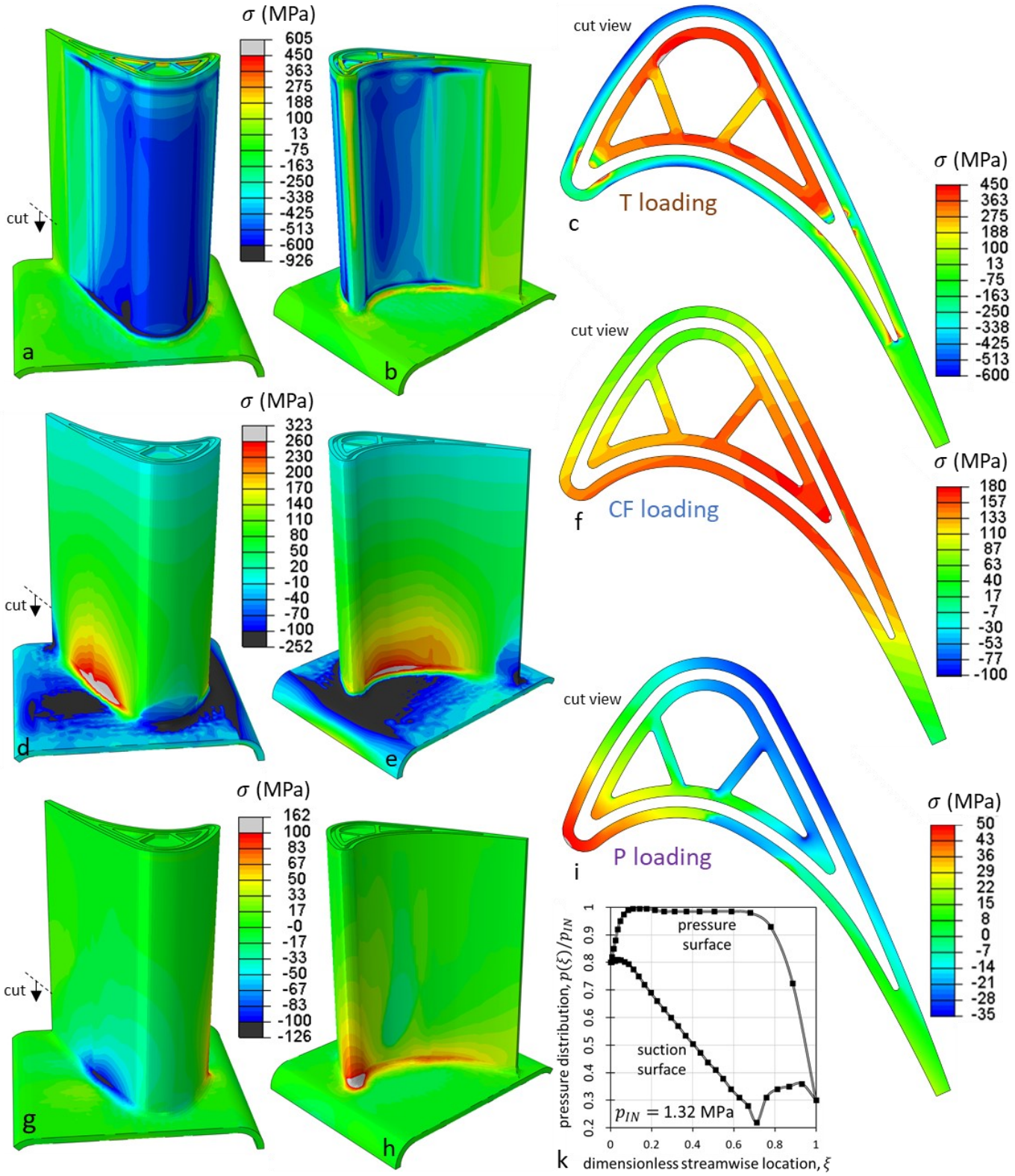

Figure 4. Turbine blade stress field under thermal (T) loading (a-c), centrifugal (CF) loading (d-f) and gas pressure (P) loading (g-i). (k) shows the gas pressure distribution and (c), (f), (i) show stresses at the blade cross-section cut denoted in (a). Maximum absolute principal stresses are used in the contours. Maximum absolute principal stress, $\sigma = max\langle|\sigma_1|, |\sigma_2|, |\sigma_3|\rangle$, contours are used.

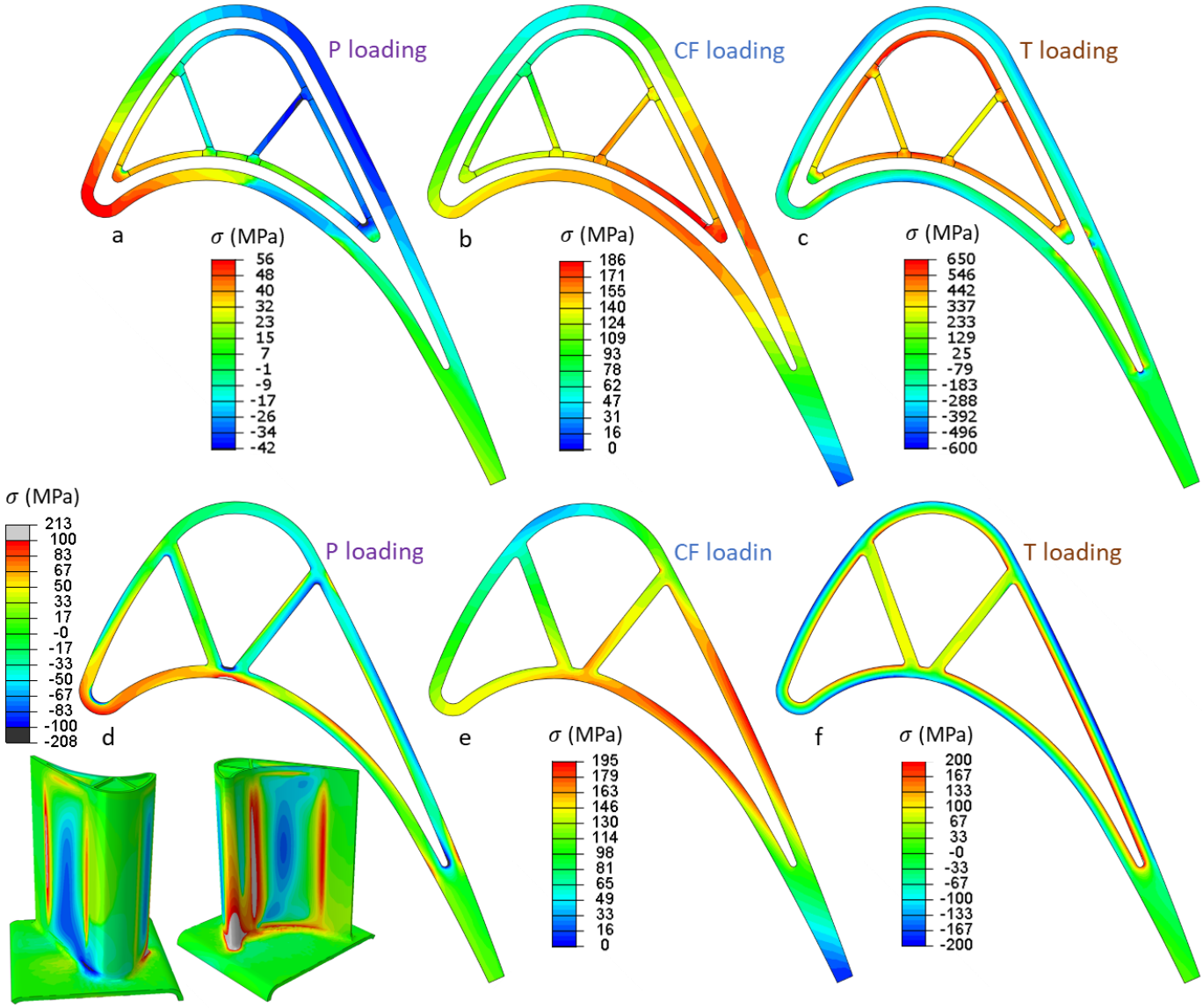

Figure 5. Stress field at the turbine cross-section cut denoted in Fig 4a for gas pressure (P) loading (a), thermal (T) loading (b) and centrifugal (CF) loading (c) for a wall thickness ratio $t_c/t_h = 0.5$. Corresponding stresses for a single wall turbine blade are shown in (d-f). Maximum absolute principal stress, $\sigma = max\langle|\sigma_1|, |\sigma_2|, |\sigma_3|\rangle$, contours are used.

4. Nominal stresses in DWTC systems

4.1 Outline

In this section we develop theoretical-FE solutions for nominal stresses in 2D and 3D idealised double wall geometries with discrete pedestals, where T loading and CF loading occur

simultaneously. These solutions provide an understanding of the relationship between stress and geometry and help identify the boundary conditions that should be applied in a repeating block in order to capture the CF-T loading response of a turbine blade. Once the boundary conditions are justified, we then examine the nominal stress field in the unit cell of 1b.

4.2 General solution for 2D flat walls

We first examine the 2D plane stress model in Fig 6a, mounted at one end (left) and rotating with velocity, ω (rad/s), about the engine axis (parallel to the z axis and located virtually at point C); the latter is at distance, R_{tip}, from the free end/tip. The temperatures $T_{max} > T_{med_h} > T_{med_c} > T_{min}$ apply uniformly along the body length, L, giving average wall temperatures, $T_h = 0.5(T_{max} + T_{med_h})$, $T_c = 0.5(T_{med_c} + T_{min})$. t_h, t_c are the wall thicknesses and Z, S, H, D_{ped} denote pedestal distance, spacing, height and diameter ($Z = S + D_{ped}$). Because $t_h + t_c + H << R_{tip}$ here, the centrifugal force vectors, dF_y, are negligible, such that for an infinitesimal mass, dm, at distance, r, from C the relation $dF_x \approx dF = dm\, r\, \omega^2$ holds. The stresses at a position, R_x, where perturbation effects from the pedestals and the end condition diminish, are determined by:

$$\underline{\textit{Kinematics}}$$

$$\kappa_h = \kappa_c = \kappa \;\rightarrow\; \frac{M_h}{EI_h} + \frac{a\Delta T_{hwall}}{t_h} = \frac{M_c}{EI_c} + \frac{a\Delta T_{hcool}}{t_h} \quad (a)$$

$$\bar{\varepsilon}_h - \bar{\varepsilon}_c = H_c\kappa \;\rightarrow\; \frac{N_h}{Et_h} + a(T_h - T_c) - \frac{N_c}{Et_c} = H_c\frac{M_c}{EI_c} \quad (b)$$

(1)

$$\underline{\textit{Equilibrium}}$$

$$\textit{(forces)}\;\; N_h + N_c = F_{hwall} + F_{cwall} + F_{ped} \quad (c)$$

$$\textit{(moments)}\;\; M_h + M_c + N_cH_c = -H_cF_{cwall} - 0.5(H + t_h)F_{ped} \quad (d)$$

where κ_h, κ_c, are the total bending curvatures of the walls, $\bar{\varepsilon}_h$, $\bar{\varepsilon}_c$ are the membrane strains (at mid-plane of each wall), $H_c = H + 0.5(t_h + t_c)$ is the wall mid-plane separation of the walls, M_h, M_c are the (internal) bending moments per unit length, N_h, N_c, are the (internal) membrane forces per unit length, I_h, I_c are the second moments of areas per unit length, F_{hwall}, F_{cwall} are the (external) CF forces generated at R_x due to the inertia of each wall corresponding to a length, $L_x = R_{tip} - R_x$, and F_{ped} is the CF force due to the inertia of the pedestals. The CF forces are deduced as:

$$F_{wall} = \int_{R_x}^{R_{tip}} dm\, r\, \omega^2 dr = \rho\, \omega^2 A_{wall}\, \tilde{L}_x \qquad (a)$$

(2)

$$F_{ped} = \rho\, \omega^2\, V_{ped} \sum_{i=1}^{n} R_{ped_i} = \rho\, \omega^2 V_{ped} \left\{ \frac{L_x}{Z} \left[R_{tip} + 0.5(Z - L_x) \right] \right\} \quad (b)$$

where $\tilde{L}_x = L_x\left(R_{tip} - 0.5L_x\right)$ is a length factor, A_{wall} is the hot or cool wall cross-sectional area, V_{ped} is the volume of each pedestal, R_{ped_i} is the distance of the centre of each pedestal from C and n is the total number of pedestals within the length L_x. The final form of Eq (2b) is derived by considering:

$$\sum_{i=1}^{n} R_{ped_i} = n(R_{tip} - L_x) + S \sum_{i=1}^{n} i = n(R_{tip} - L_x) + 0.5\, S[n(n+1)] \qquad (3)$$

with $n = L_x/S$. The nominal stresses, $\sigma(\hat{y})$ as a function of through thickness position, $\hat{y}$, in each wall are found by substituting the solution of Eqs (1) in terms of N_h, N_c, M_h, M_c into the classical beam equation, $\sigma(\hat{y}) = M\hat{y}/I + N/t$.

As mentioned in the introduction, our previous 2D thermal stress analysis [33] assumed that $\Delta T_{ped} = T_{med_h} - T_{med_c} = 0$ and that $\Delta T_{cwall} = T_{med_c} - T_{min} = 0$ and indicated that in such cases the hot wall experiences much higher stresses than the cool wall [33]. For the more realistic case here ($\Delta T_{ped} \neq 0$, $\Delta T_{cwall} \neq 0$) the thermal stress field is more complex, as it not only depends on t_c/t_h

and H but also on the fractional contributions $\overline{\Delta T}_{hwall}$, $\overline{\Delta T}_{ped}$, $\overline{\Delta T}_{cwall}$. Application of thermal loading according to Table 1 gives the thermal FE stresses shown in Fig 6b; these stresses are notably higher in the cool wall, contrary to our previous analysis for $\Delta T_{ped} = \Delta T_{cwall} = 0$ [33]; the result agrees exactly with the new theoretical solution in Eqs (1) (not shown). CF loading includes the additional effect that the CF stresses carried by the walls increase with pedestal height, H, and/or pedestal diameter, D_{ped}, and/or narrower pedestal distances Z. In addition, Eq (1d) implies that for $t_c \neq t_h$ the bending moment, $0.5(H + t_h)F_{ped}$, caused by the inertia of the pedestals will cause bending of the system. This is indeed evidenced by the FE solution for CF loading shown in Fig 6c based on the CF loading values in Table 1.

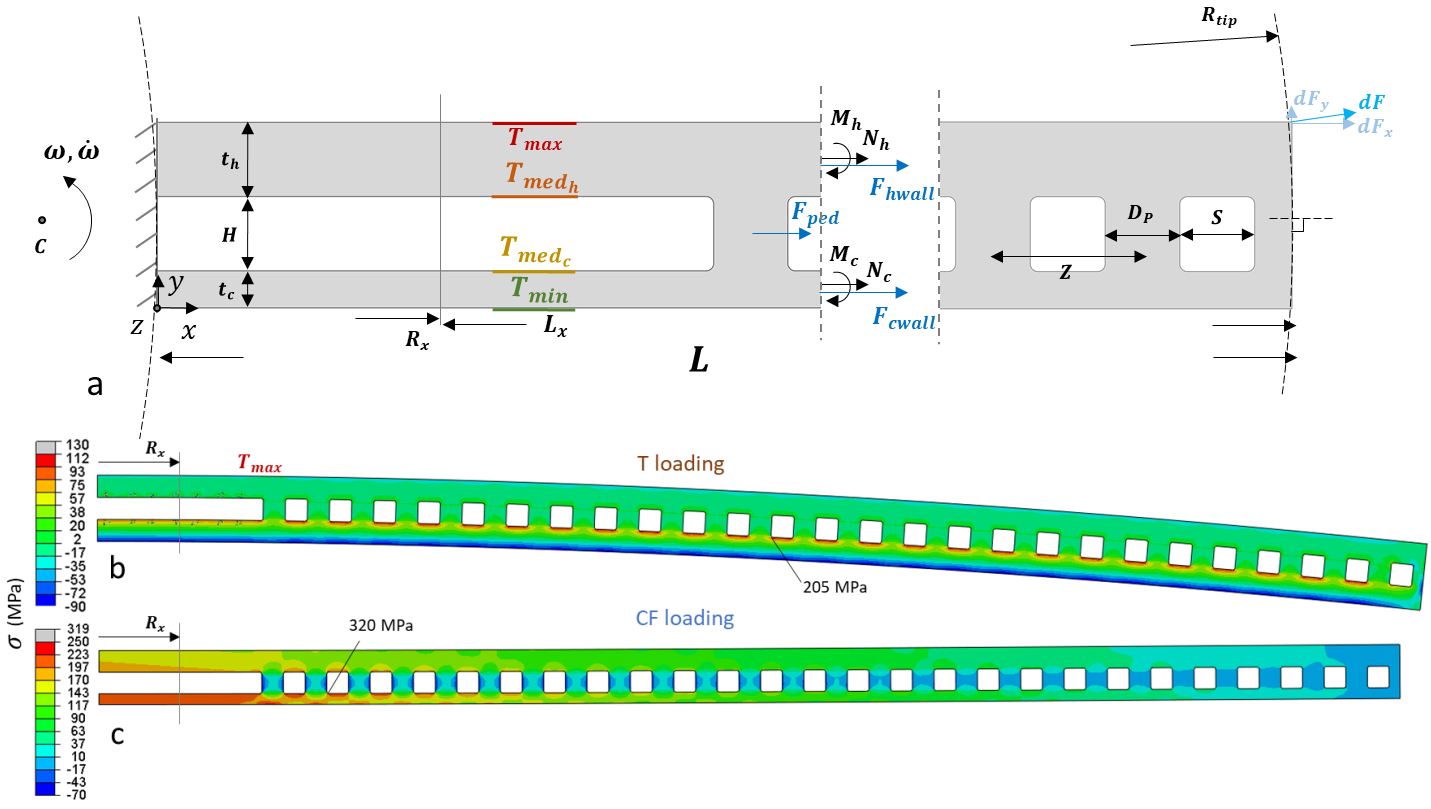

Figure 6. (a) 2D idealisation of flat double walls with thermal (T) and centrifugal (CF) loading and dimensions denoted; dashed lines denote cuts across the thickness of the system; C represents the centre of rotation. Stress fields under T loading and CF loading are shown in (b-c), respectively; (c) highlights that bending of the system occurs for CF loading due to different wall thicknesses. Maximum absolute principal stress, $\sigma = max\langle|\sigma_1|, |\sigma_2|, |\sigma_3|\rangle$, contours are used.

All the above indicate that several effects need to be considered when minimising stresses through changing geometry for combined T-CF loading. Most of the effects however arise in the general case of flat walls with free ends where non-zero wall rotations can occur [34], which is not the case in a turbine blade [34].

4.3 Solution for 3D cylindrical walls

We now analyse a particular 3D case of more relevance to the turbine blade of Fig 3, which consists of cylindrical double walls [34] with sufficient length and constant external radius of curvature, R. Fig 7a depicts a cylindrical segment/strip of this configuration (a ratio $R/t_h = 7.5$ is used to resemble the blade suction side curvature in Fig 3c) and Fig 7b shows the repeating unit cell; combined T-CF loading here occurs in a similar manner to Fig 6a. Here the z-rotations of the walls are prevented by cyclic symmetry, i.e. zero θ-displacements at planes $\bar{\theta} = 0$ and $\bar{\theta} = 1$, and the θ-rotations are also prevented along almost the entire length, L. The latter owes to the fact that θ-rotations would inevitably imply radial r −deflections and therefore hoop strains; the high resistance of the geometry against these hoop strains only allows them to occur (along with θ-rotations) near the cylindrical tip (near R_{tip} in Fig 7a) [52], which is a local effect and does not correspond to a region of interest (CF stresses are zero at the tip). The above conditions of zero wall rotations are evidenced in the FE solutions of Fig 7c-d for pure T loading and pure CF loading, respectively. In these solutions we constrain only z-displacements at the $r - \theta$ plane, to avoid localised r-deflections that would occur if fixed boundary conditions were applied (depending on the R/t_h ratio), which would complicate the stress field near position R_x (see Fig 7a).

By updating the kinematic equations (Eqs (1a-b)) to account for the Poisson's ratio, ν, effect and by postulating zero total bending curvatures, the theoretical 2D solution (Eqs (1)) for flat walls, based on classical beam theory, can be extended into an approximate 3D solution for cylindrical walls, based on flat plate theory; the solution is provided in Appendix D [34]. The solution is exact for flat

systems (and cylindrical systems of $R/t \to \infty$) and remains an accurate approximation for cylindrical systems of low curvature, i.e. $R/t > 20$ [34]. At lower R/t, the variation of nominal stresses along the wall planes and the non-linearity in the through thickness stress distributions become important [34], and therefore the solution is no longer accurate. The theoretical solution is therefore useful in highlighting the 1st order features of the response for flat walls with constrained rotations, and the way in which the external CF forces are applied. A key element of the solution for this study is that the inertia of pedestals adds a CF force, F_{ped}, to the walls, whereas a CF force, F_{holes}, must be deducted to account for the presence of film and impingement holes.

Prior to calculating F_{holes}, we first verify that by determining analytically the force, $F_{walls} + F_{ped}$, at a given location, R_x, in Fig 7a and then applying it as a boundary condition in the unit cell (Fig 7b), we obtain the same FE stress field as using the large scale model (Fig 7a) for the corresponding R_x location. By using $V_{ped} = 0.25\,\pi H {D_{ped}}^2$ in Eq (2b) and using Eq (2a) for both walls, we get $F_{walls} + F_{ped} = \rho\,\omega^2 \tilde{L}_x A_{walls} + \rho\,\omega^2 V_{ped}\,\frac{L_x}{Z}\left(R_{tip} + 0.5(Z - L_x)\right)$. Normalising this total force by A_{walls} gives the CF stress, σ_{CF}, which we apply as a normal surface traction uniformly at the $\bar{z} = 1$ plane in Fig 7e (CF loading parameters are given in Table 1); the latter corresponds to 1/4 of the unit cell in Fig 7b and involves zero θ-displacements at the $\bar{\theta} = 0$ and $\bar{\theta} = 1$ planes and zero z-displacements at the $\bar{z} = 1$ plane. We also apply the inertial forces associated with the mass of the unit cell of Fig 7e itself. Indeed, the stress field in Fig 7e is practically the same as the stress field surrounding the fifth pedestal in Fig 7d, for which the calculations were performed. This agreement adds credibility to the analysis and indicates that the details of T-CF stresses can be conveniently assessed by using repeating block models.

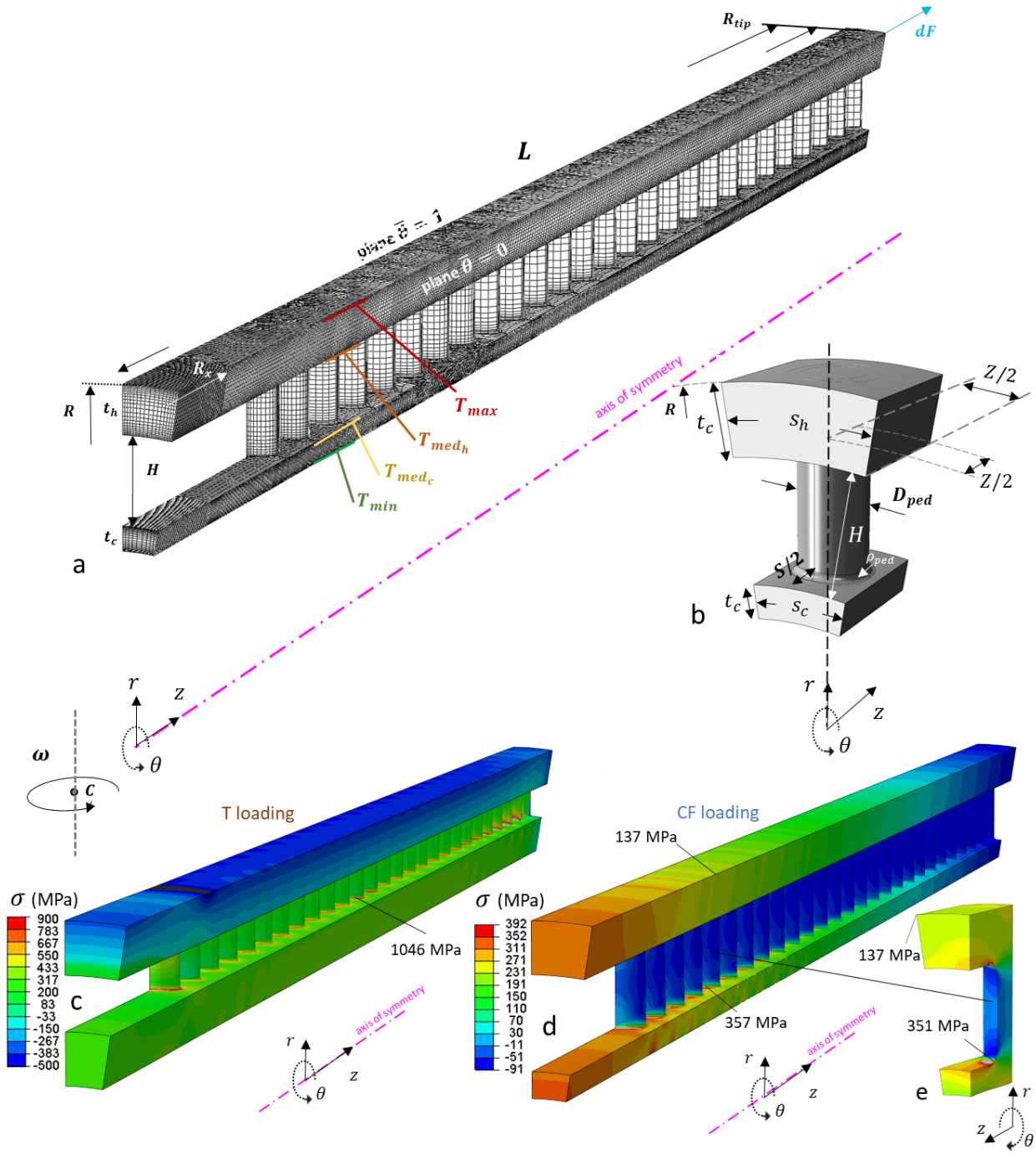

Figure 7. (a) 3D cylindrical double wall FE model with thermal (T) and centrifugal (CF) loading and dimensions; a segment of the cyclically symmetric geometry is used. (b) Repeating unit cell of the geometry in (a), with detailed dimensions. Stress fields under thermal loading and centrifugal loading are shown in (c-d), respectively. (e) shows stresses in a unit cell due to z-tractions applied on the wall cross-sections to simulate centrifugal loading. Geometric parameters and thermal-centrifugal loading parameters for Fig 7c are given in Table 1; CF loading in Fig 7d involves $t_c = 0.5t_h$, $H = 2t_h$ and $t_h =$ 1mm. Maximum absolute principal stress, $\sigma = max\langle|\sigma_1|, |\sigma_2|, |\sigma_3|\rangle$, contours are used.

4.4 Solution for the 3D flat unit cell

We now analyse the details of the stress field for the unit cell of Fig 1b. The flat geometry used here allows for an understanding of the detailed nominal stress characteristics and stress concentrations with greater ease than cylindrical geometries. This is because the theoretical solution in Appendix D gives the same nominal wall stresses with the FE model in Fig 1b (without holes), provided that the wall rotations at the boundaries of the FE model are constrained and that the θ axis in Appendix D is equivalent to the x axis in Fig 1b.

The nominal stresses in the z direction at each wall surface of Fig 1b read:

$$\sigma_{T_{max_z}} = \frac{0.5Ea\Delta T}{1-\nu}\left[-\overline{\Delta T}_{hwall} - \bar{t}_c\left(\overline{\Delta T}_{ped}+1\right)\right] \quad + (\rho+\rho^*)\,\omega^2\tilde{L}_x \qquad (a)$$

$$\sigma_{T_{med_{h_z}}} = \frac{0.5Ea\Delta T}{1-\nu}\left[\overline{\Delta T}_{hwall} - \bar{t}_c\left(\overline{\Delta T}_{ped}+1\right)\right] \quad + (\rho+\rho^*)\,\omega^2\tilde{L}_x \qquad (b)$$

$$\sigma_{T_{med_{c_z}}} = \frac{0.5Ea\Delta T}{1-\nu}\left[-\overline{\Delta T}_{cwall} + \bar{t}_h\left(\overline{\Delta T}_{ped}+1\right)\right] \quad + (\rho+\rho^*)\,\omega^2\tilde{L}_x \qquad (c) \qquad (4)$$

$$\sigma_{T_{min_z}} = \frac{0.5Ea\Delta T}{1-\nu}\left[\overline{\Delta T}_{cwall} + \bar{t}_h\left(\overline{\Delta T}_{ped}+1\right)\right] \quad + (\rho+\rho^*)\,\omega^2\tilde{L}_x \qquad (d)$$

where $\bar{t}_h = t_h/(t_c+t_h)$ and $\bar{t}_c = t_c/(t_c+t_h)$ are the contributions of hot and cool wall thicknesses to the total thickness, t_c+t_h, and ρ^* is an 'equivalent' density determined by $\rho^*\omega^2\tilde{L}_x = (F_{ped} - F_{holes})/4s(t_h+t_c)$, which induces an increase or decrease in CF stresses depending on the total volume of pedestals in comparison to the total volume of holes in the system. The calculation of F_{ped} and F_{holes} for the model of Fig 1b is given in Appendix E. The corresponding θ-stresses are given by Eqs (4a-c) without the $(\rho+\rho^*)\,\omega^2\tilde{L}_x$ terms. This implies that:

a) for flat walls the nominal stresses are determined by the superposition of equibiaxial thermal (T) stresses with uniaxial CF stresses along the z axis,

b) for combined CF-T loading, $\left|\sigma_{T_{max}z}\right| < \left|\sigma_{T_{max}\theta}\right|$ always occurs at the outer surface of the hot wall hole and $\sigma_{T_{med_c}z} > \sigma_{T_{med_c}\theta}$ always holds at the inner surface of the cool wall.

The latter is on the grounds that T stresses in the outer surface of the hot wall are always compressive (see Eq (4a)) and thus reduce in the z direction due to tensile CF loading, whereas T stresses in the inner surface of the cool wall are practically always tensile and increase further with CF loading along the z axis. The maximum tensile T stresses occur at the outer surface of the cool wall (where T_{min} occurs) whereas Eq (4b) indicates that T stresses at the hot wall inner surface will be compressive for high $\overline{\Delta T}_{ped}$ and/or high $\bar{t}_c$ values and tensile when $\overline{\Delta T}_{hwall}$ dominates over $\overline{\Delta T}_{ped}$ and/or at low $\bar{t}_c$. We can also identify the crucial effect that by reducing $\bar{t}_c$, and thus increasing $\bar{t}_h$, less severe compressive T stresses occur at the hot wall outer surface (Eq (4a)) and higher tensile T stresses at the cool wall surfaces (Eqs (4c-d)). The fact that all the above key effects are immediately identified by an observation of Eqs (4) is one of the merits of the theoretical solution in Appendix D.

For clarity, we also plot the FE solution for the T stress field in Figs 8a-b. The FE model here uses 1/8 of Fig 1b. The T loading conditions are given in Table 1 and we apply zero x-displacements at $\bar{x} = 0$, zero z-displacements at $\bar{z} = 1$, common z-displacements at $\bar{z} = 0$ and common x-displacements at $\bar{x} = 1$ (see Fig 8a). For CF loading we apply uniformly a z-traction of $(\rho + \rho^*)\,\omega^2 \tilde{L}_x$ at the cross-sections of the walls, at $\bar{z} = 0$ (dashed regions in Fig 8b). This assumes that the inertia of the pedestals that are present in the unit cell (Fig 8b) have a minor influence on stresses. This is indeed true, since an independent FE analysis of a unit cell with a full pedestal under CF stresses induced by the inertia of the unit cell itself, shows a peak stress of only 16 MPa in Fig 8c; here we use zero x-displacements at $\bar{x} = 0$, zero z-displacements at $\bar{z} = 0$, common z-displacements at $\bar{z} = 1$ and common x-displacements at $\bar{x} = 0$, whereas inertia forces are based on the parameters of Table 1. For these parameters the small stress value is indeed expected; for

example, a crude calculation of the shear stress, τ, along each pedestal-wall intersectional area, A_{ped}, gives $\tau = \rho\,\omega^2 V_{ped} R_{tip}/2A_{ped} = 1.3$ MPa.

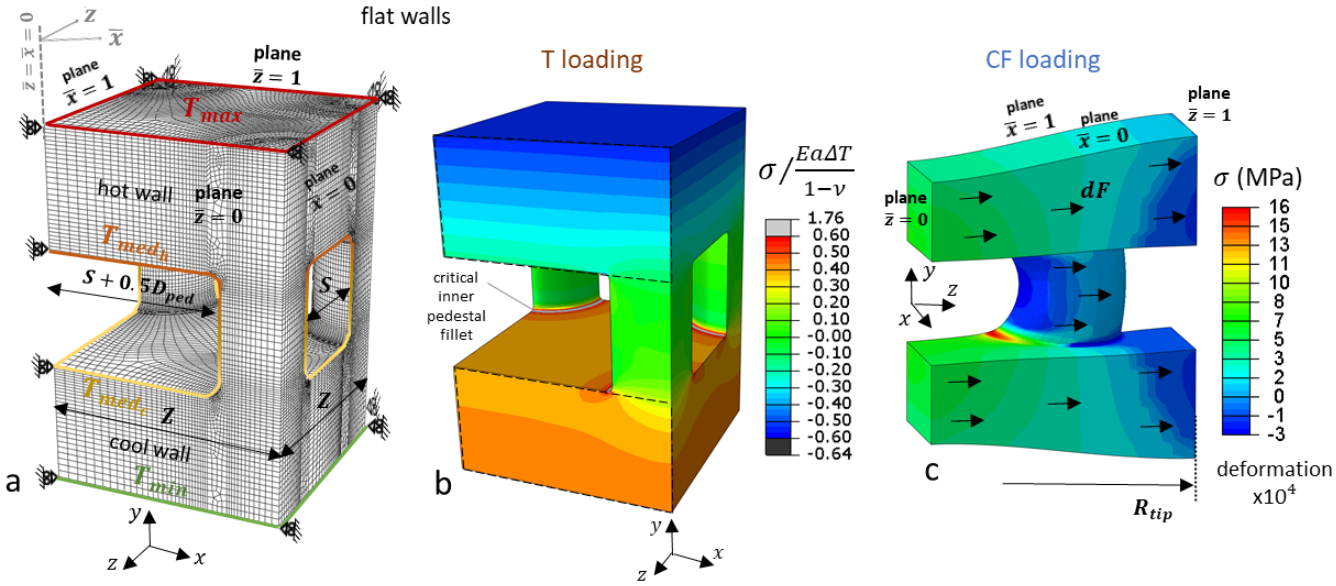

Figure 8. (a) 3D flat double wall FE model with thermal (T) and kinematic boundary conditions denoted, along with dimensions; the model corresponds to 1/8 of Fig 1b without holes. (b) Maximum absolute principal stress, $\sigma = max\langle|\sigma_1|, |\sigma_2|, |\sigma_3|\rangle$, contours, normalised by the thermal loading factor, $EaΔT/(1-\nu)$. (c) Stresses in a full-pedestal unit cell due to centrifugal forces associated with the inertia of the unit cell.

5. Peak stresses in DWTC systems

5.1 Outline

Following the verification of boundary conditions and the understanding of nominal stresses, this section will now examine how the stresses are magnified locally at holes and pedestals by a stress concentration factor, SCF. The latter is defined here as the ratio of actual stress in the vicinity of the feature divided by the nominal stress at the corresponding location when the feature is absent. The sensitivity of peak stresses to the wall thickness ratio and the T-CF loading conditions are investigated.

5.2 The stress concentration factor

The peak stress, σ, in the vicinity of a hole or pedestal is given by the superposition:

$$\sigma = \sigma_T \mathrm{SCF_T} + \sigma_{CF} \mathrm{SCF_{CF}} \tag{5}$$

where σ_T, $\mathrm{SCF_T}$ denote the nominal stress and stress concentration factor for pure T loading, whereas σ_{CF}, $\mathrm{SCF_{CF}}$ are the corresponding values for CF loading ($\sigma_{CF} = (\rho + \rho^*)\, \omega^2 \tilde{L}_x$). $\mathrm{SCF_T}$ and $\mathrm{SCF_{CF}}$ are different here because T loading is equibiaxial i.e. stress state, $\sigma_\theta/\sigma_z = 1$, whereas CF is uniaxial i.e. $\sigma_\theta/\sigma_z = 0$. To demonstrate the high sensitivity of SCF with respect to σ_θ/σ_z, we use the FE model in Fig 8b to compare maximum $\mathrm{SCF_{CF}}$ and $\mathrm{SCF_T}$ values at the inner pedestal fillet for a range of pedestal diameters, D_{ped}/t_h, and fillet radii, ρ_{ped}/t_h (fixed $t_h = t_c = H = 1$ mm). Fig 9a shows that always $\mathrm{SCF_{CF}} > \mathrm{SCF_T}$ and that both $\mathrm{SCF_{CF}}$ and $\mathrm{SCF_T}$ decrease with ρ_{ped}/t_h and increase with D_{ped}/t_h, in agreement with [33]. When $\sigma_\theta/\sigma_z = 1$ (T loading) the max $\mathrm{SCF_T}$ is observed to apply uniformly along the circumference of the pedestal fillet, whereas when $\sigma_\theta/\sigma_z = 0$ (CF loading), the max $\mathrm{SCF_{CF}}$ is confined within a small region of the circumference (at the $\bar{z} = 1$ plane of Fig 8b). This explains why $\mathrm{SCF_{CF}} > \mathrm{SCF_T}$ and suggests that CF loading and T loading alone give the upper and lower bounds of SCF.

To verify this, we examine whether the SCF for any combination of T-CF loading obeys the linear relation:

$$\mathrm{SCF} = (\mathrm{SCF_T} - \mathrm{SCF_{CF}})\, \sigma_\theta/\sigma_z + \mathrm{SCF_{CF}} \tag{6}$$

where here σ_θ/σ_z is that for the inner cool wall surface (as this is relevant to the inner pedestal fillet), and is given by:

$$\sigma_\theta/\sigma_z = \sigma_{T_{med_c}\theta}/\sigma_{T_{med_c}z} = \frac{0.5\left[-\overline{\Delta T}_{cwall} + \bar{t}_h\left(\overline{\Delta T}_{ped} + 1\right)\right]}{0.5\left[-\overline{\Delta T}_{cwall} + \bar{t}_h\left(\overline{\Delta T}_{ped} + 1\right)\right] + \frac{1}{\lambda}} \tag{7}$$

where, λ, quantifies the severity of T loading with respect to CF loading according to:

$$\lambda = \frac{Ea\Delta T/(1-\nu)}{(\rho + \rho^*)\, \omega^2 \tilde{L}_x} \tag{8}$$

By applying Eq (7) for two values of λ (7.1 and 1.77) and using Eq (6) along with known values of $\mathrm{SCF_{CF}}$ and $\mathrm{SCF_T}$ from Fig 9a, and then multiplying SCF with $\sigma_{T_{med_{c_z}}}$ defined by Eq (4c), we obtain the dashed curves in Fig 9(b). These curves agree closely with the direct FE solution for combined T-CF loading, adding validity to Eq (6).

In addition to the strong SCF$-\sigma_\theta/\sigma_z$ relation, the SCF also depends on the contributions of membrane forces and bending moments to the critical nominal stress in the vicinity of a surface, quantified here by the stress distribution factor, $\bar{\sigma}/\sigma$, which normalises the average nominal thermal stress through the wall, $\bar{\sigma}$, by the nominal thermal surface stress, σ. The analytical expression of $\bar{\sigma}/\sigma$ for each wall surface of Fig 1b is provided in Appendix F, along with an explanation of the theoretical range, $\infty < \bar{\sigma}/\sigma < -\infty$. The practical range of $\bar{\sigma}/\sigma$ here is quite narrow. For the thermal loading parameters of Table 1 we get $(\bar{\sigma}_\theta/\sigma_\theta)_{T_{max}} = 0.68$ (combined compression with bending), $(\bar{\sigma}_z/\sigma_z)_{T_{med_c}} = 1.06$ and $(\bar{\sigma}_z/\sigma_z)_{T_{min}} = 0.95$ (tension with negligible bending), since the thermal gradient across the cool wall is negligible, i.e. $\overline{\Delta T}_{cwall} = 0.045$. For $\overline{\Delta T}_{ped} = 1$ (and thus $\overline{\Delta T}_{hwall} = 0$) we get $\bar{\sigma}_\theta/\sigma_\theta = -1$ (pure compression) always and for $\overline{\Delta T}_{hwall} = 1$ (and thus $\overline{\Delta T}_{ped} = 0$), $\bar{\sigma}_\theta/\sigma_\theta$ depends on $\bar{t}_c$. When $\bar{t}_c \to \infty$, $\bar{\sigma}_\theta/\sigma_\theta = -1$, regardless of $\overline{\Delta T}_{ped}/\overline{\Delta T}_{hwall}$.

Bending here occurs only under T loading and therefore the factor, $\bar{\sigma}/\sigma$, influences only $\mathrm{SCF_T}$. We can now use the same approach as in Eq (6) and assume that the $\mathrm{SCF_T} - \bar{\sigma}/\sigma$ relation obeys the linear form:

$$\mathrm{SCF_T} = \frac{\left(\mathrm{SCF_{T_2}} - \mathrm{SCF_{T_1}}\right)}{(\bar{\sigma}/\sigma)_2 - (\bar{\sigma}/\sigma)_1}(\bar{\sigma}/\sigma - (\bar{\sigma}/\sigma)_1) + \mathrm{SCF_{T_1}} \tag{9}$$

where the $\mathrm{SCF_{T_1}}$ and $\mathrm{SCF_{T_2}}$ values are obtained by two FE simulations of T loading for different $(\bar{\sigma}/\sigma)_1$ and $(\bar{\sigma}/\sigma)_2$ i.e. different values of $\overline{\Delta T}_{ped}$ (or equivalently different $\overline{\Delta T}_{ped}/\overline{\Delta T}_{hwall}$). These values are given in Table 3 for the four critical locations of the system, along with $\mathrm{SCF_{CF}}$ values obtained by an additional FE simulation under CF loading alone. Table 3 shows that $(\bar{\sigma}_\theta/\sigma_\theta)_{T_{max}} =$

0.35 gives $\mathrm{SCF}_{\mathrm{film_T}} = 3.71$, whereas $(\bar{\sigma}_\theta/\sigma_\theta)_{T_{max}} = 0.79$ leads to $\mathrm{SCF}_{\mathrm{film_T}} = 4.57$, highlighting that increasing the membrane force increases the max SCF at the outer acute wedge-vertex of the film hole.

Using Eq (9) with the values of Table 3, and then feeding the resulting value of $\mathrm{SCF_T}$ together with $\mathrm{SCF_{CF}}$ from Table 3 into Eq (6) to give the overall SCF and combining this with the nominal thermal stresses, σ_T, and CF stress, σ_{CF} (from Eq (4)), we can predict peak stresses. Predictions can be made for any combination of the three critical parameters of the problem $-$ λ, $\overline{\Delta T}_{ped}$ (or equivalently the ratio $\overline{\Delta T}_{ped}/\overline{\Delta T}_{hwall}$ since $\overline{\Delta T}_{cwall} = 0.045$ is fixed), and t_c/t_h (or equivalently the ratios $\bar{t}_c$, $\bar{t}_h$).

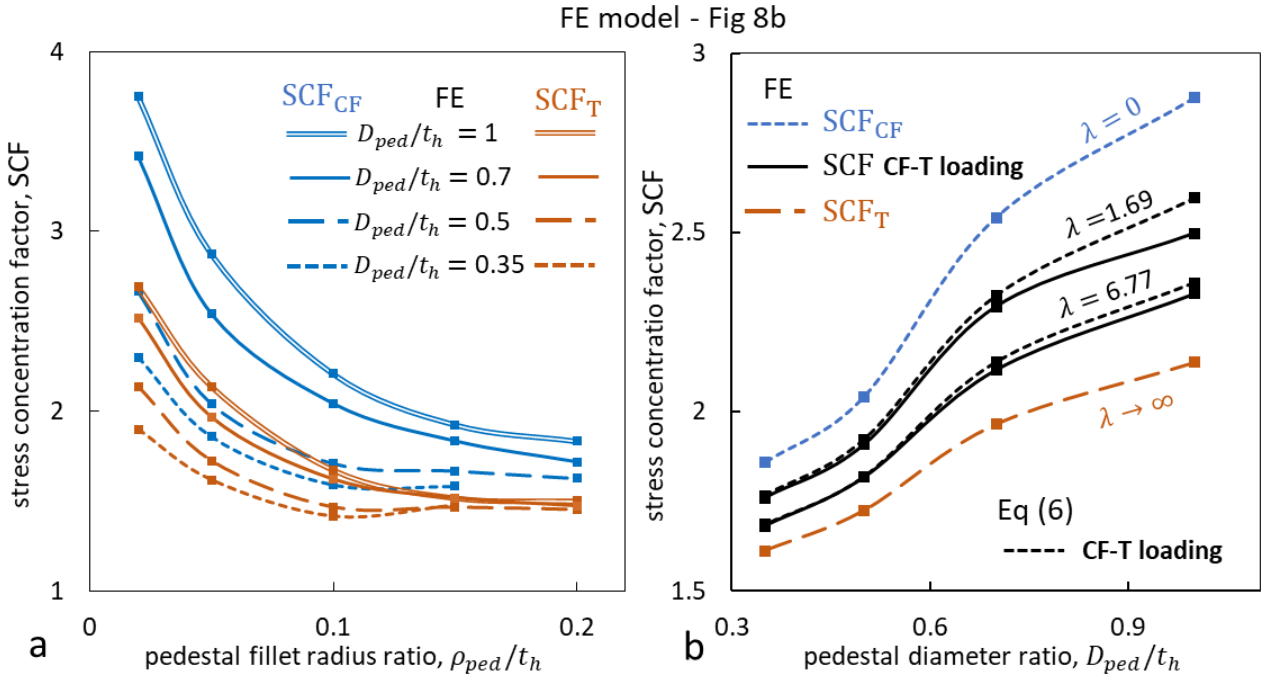

Figure 9. (a) FE solutions for SCF at the inner pedestal fillet of the model of Fig 8a versus pedestal fillet radius ratio for varying pedestal diameter ratios, for pure centrifugal (CF) and pure thermal (T) loading, respectively; pedestal spacing, S, which is changed together with D_{ped} according to $S = D_{ped}$. (b) FE solutions and Eq (6) predictions for SCF at the same location for two centrifugal-thermal loading combinations, corresponding to factors, $\lambda = 1.69$ and $\lambda = 6.77$.

Table 3. Reference SCF values for pure thermal (T) and pure centrifugal (CF) loading.

		film hole outer acute wedge-vertex		film hole inner acute wedge-vertex		impingement hole		critical inner pedestal fillet	
T loading	SCF_{T_1}, SCF_{T_2}	3.71	4.57	8.9	5.78	1.95	1.85	1.96	1.81
	$(\dot{\sigma}/\sigma)_1$, $(\dot{\sigma}/\sigma)_2$	0.35	0.79	3.3	1.35	0.95	0.96	1.06	1.04
	$\overline{\Delta T}_{ped}$	0.2	0.8	0.58	0.8	0.2	0.8	0.2	0.8
	CF loading	$SCF_{CF} = 7.03$		$SCF_{CF} = 7.1$		$SCF_{CF} = 3.35$		$SCF_{CF} = 3.18$	

5.3 FE-theoretical solutions for peak stresses

The accuracy of the framework of Section 5.2 is assessed in Fig 10, by comparing the predictions of Eq (5) against direct FE solutions for combinations of λ, $\overline{\Delta T}_{ped}$ and t_c/t_h; characteristic FE stress fields are illustrated in Figs 11-12. Fig 12 shows a close overall agreement between Eq (5) and FE results. Some discrepancies between the FE result and Eq (5) arise from the fact that the SCF at the impingement hole and pedestal changes slightly with t_c, whereas we only used three reference SCF values for each location in Eq (5) (taken for $t_c/t_h = 0.5$), for the purpose of the theoretical analysis. Both calculations highlight the linear variation of stresses with $\overline{\Delta T}_{ped}$ for fixed λ and t_c/t_h, which can be explained by Eqs (5, F1, 9). Eq (5) provides conservative predictions only in Figs 12c,f,i, which corresponds to extreme CF loading corresponding here to $\omega = 16378$ rpm and a blade tip velocity of 2 Mach based on a fixed $R_{tip} = 400$ mm.

Weight should be given to the practical case of combined T-CF loading with $\lambda > 6.48$ (Figs 10b,e,h), associated with $\omega = 857.5$ rad/s (equivalent to 8188 rpm and tip velocity of 1 Mach). Here the nominal CF stresses, $\sigma_{CF} = (\rho + \rho^*)\,\omega^2 \tilde{L}_x$, increase from 111 MPa for $t_c/t_h = 1$ up to 115 MPa for $t_c/t_h = 0.2$. Note that since ρ^* decreases with $t_h + t_c$ (Section 4.4), λ increases with t_c/t_h (Eq (8)) due to the inertia of features; however, the effect on σ_{CF} is evidently small. A key trend in Figs 10b,e,h is that low t_c/t_h, and/or an enhanced $\overline{\Delta T}_{ped}$, both reduce compression at the outer acute wedge-vertex of the film hole at the cost of increasing the tension at internal features, i.e. the

impingement hole and inner pedestal fillet; the same effects occurs for pure T loading (Figs 10a,d,g). The increase of tensile stresses at the internal features due to reducing t_c/t_h and/or increasing $\overline{\Delta T}_{ped}$ is dominated by the increase of nominal tensile stresses. This is because the fixed small value of $\overline{\Delta T}_{cwall} = 0.045$ used here implies that pure tension always dominates in the cool wall i.e. $\bar{\sigma}/\sigma \approx 1$ (explained in Section 5.2.1). On the other hand, the reduction of compression at the outer acute wedge-vertex of the film hole due to reducing t_c/t_h and/or increasing $\overline{\Delta T}_{ped}$ is largely due to the reduction of $\mathrm{SCF}_{\mathrm{film}}$, along with the decrease of nominal compressive stresses.

For both the cases of pure T loading (Figs 10a,d,g) and T-CF loading for $\lambda > 6.48$ (Figs 10b,e,h), the critical stress at the inner acute wedge-vertex of the film hole switches from compression to tension with increasing $\overline{\Delta T}_{ped}$. For the particular case of $t_c/t_h = 0.2$ in Fig 10h, the maximum compressive stress occurs at the outer film hole rim between the acute wedge-vertex and the elliptical co-vertex, as indicated in Fig 12a; this occurs due to the much higher nominal stresses in the x direction (θ direction for cylindrical walls) compared to the z direction. Such nominal stress states are beneficial to performance because the SCF at the film hole rim decreases from its maximum value at the acute wedge-vertex to a minimum value at the elliptical co-vertex; these effects have been explored in [12]. For the extreme of $\lambda < 1.69$ (Figs 10c,f,i), the effects of CF loading on the resulting SCF and nominal stresses dominate, i.e. all the critical stresses become tensile (also shown in Fig 11d).

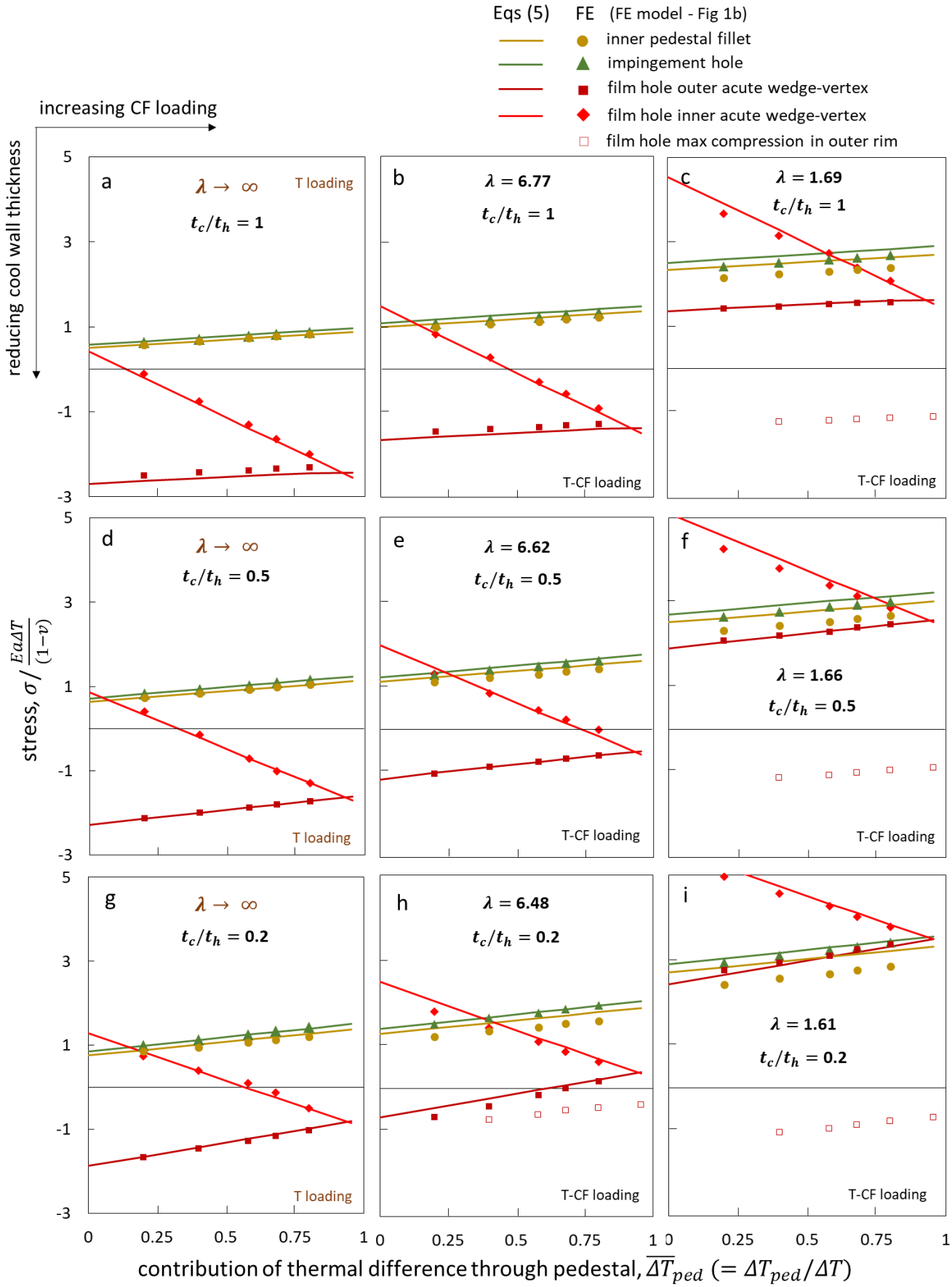

Figure 10. FE solutions and Eq (5) predictions for peak stresses at features for varying wall thickness ratio, t_c/t_h, and thermal difference contribution, $\overline{\Delta T}_{ped}$, for three situations: thermal loading (a),(d),(g), thermal loading combined with mild centrifugal loading (b),(e),(h), and thermal loading combined with extreme centrifugal loading (c),(f),(i). Maximum absolute principal stresses, $\sigma = \max\langle|\sigma_1|, |\sigma_2|, |\sigma_3|\rangle$, normalised by the thermal loading factor, $Ea\Delta T/(1-\nu)$, are used.

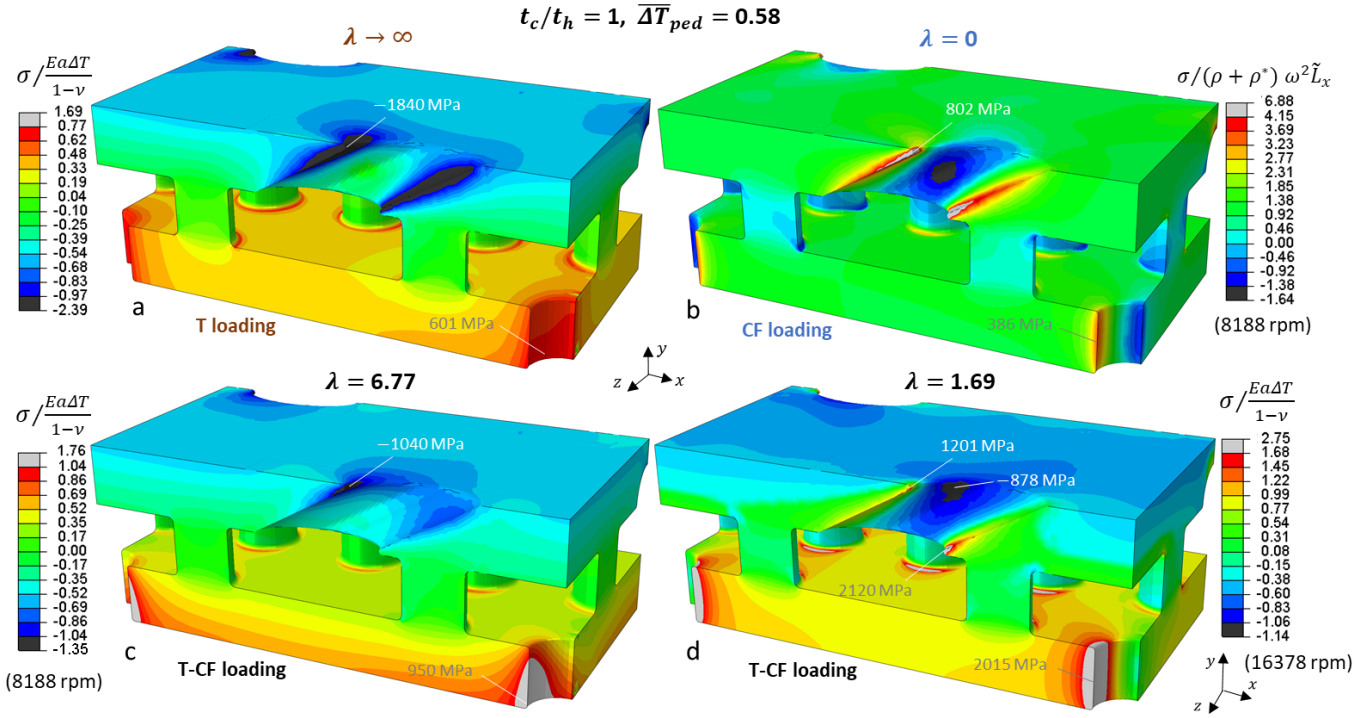

Figure 11. (a-b) Stress field in the unit cell of Fig 1b under pure thermal (T) and pure centrifugal (CF) loading, respectively (for the parameters of Table 1). (c-d) Stress field for two thermal-centrifugal loading combinations, corresponding to $\omega = 8188$ rpm (c) and $\omega = 16378$ rpm (d). CF loading involves a uniform traction at the wall sections of the $\bar{z} = 0$ plane (as described for Fig 8b in Section 4.4); we apply a traction that is slightly higher than the nominal traction, $(\rho + \rho^*)\,\omega^2\tilde{L}_x$, since the cross-sectional areas of the holes at $\bar{z} = 0$ reduces the area through which the CF load is transmitted. The locations and the values of the critical stresses at holes and pedestals are denoted. Maximum absolute principal stresses, $\sigma = \max\langle|\sigma_1|, |\sigma_2|, |\sigma_3|\rangle$, normalised by the thermal loading factor, $Ea\Delta T/(1-\nu)$, are used, except for (b) where we normalise over $(\rho + \rho^*)\,\omega^2\tilde{L}_x$.

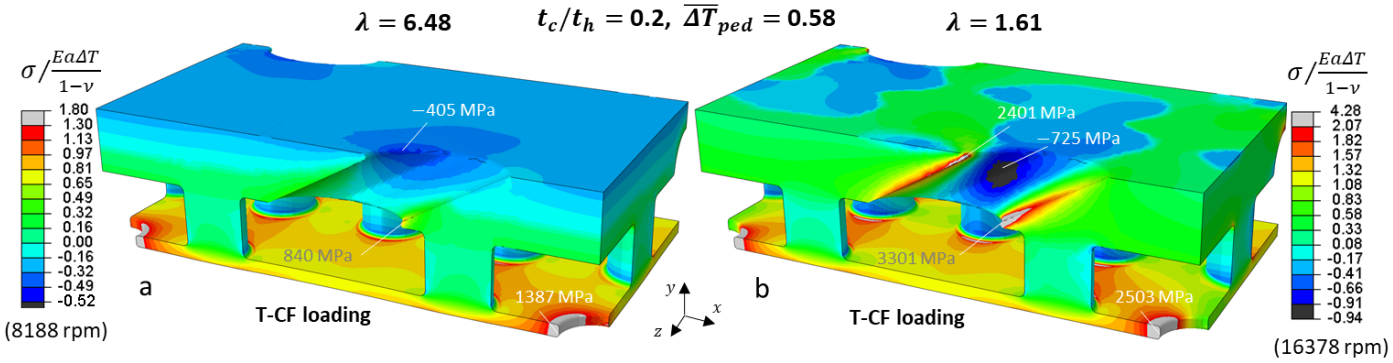

Figure 12. Stress field for the two thermal-centrifugal (T-CF) loading combinations used in Figs 11c-d, when the unit cell has a wall thickness ratio, $t_c/t_h = 0.2$ (thin cool wall); the locations and the values of the critical stresses at holes are denoted. Maximum absolute principal stresses, $\sigma = \max\langle|\sigma_1|, |\sigma_2|, |\sigma_3|\rangle$, normalised by the thermal loading factor, $Ea\Delta T/(1-\nu)$, are used.

6 Discussion

We now provide an evaluation of all our results and discuss their significance. We have shown that high stress concentration factors (SCFs) can occur at the cooling holes of double wall transpiration cooled blades, particularly at the large film hole angles considered here, where typical values of 4 and 7 occur under pure thermal (T) loading and pure centrifugal (CF) loading (Table 1). Impingement holes are transverse to the wall and thus the SCF ranges approximately between the classical theoretical values of 2 and 3, for equi-biaxial and uniaxial loading, respectively (Table 1). For well-rounded pedestal fillets the SCF falls within the lower range of $1.5 < SCF < 2$ (Fig 9). As shown recently [13], the high stresses at inclined film holes imply severe local plastic-creep deformation and thus generate concerns with respect to fatigue in the low cycle regime (LCF).

Section 5.3 highlights a key trade-off for double wall systems, in that by reducing the wall thickness ratio, t_c/t_h, critical stresses at the film hole reduce at the cost of increasing stresses at internal features, i.e. impingement holes and pedestal transitions. For pure T loading, the tensile stresses at the inner features are less severe than the compressive stresses at the film hole, such that a low t_c/t_h will likely improve the overall integrity. If severe CF loading is superimposed, and a thin cool wall is used, the compressive film hole stress can eventually take very small values, but the performance at inner features will degrade. These suggestions, however, are based on the assumption that the two loading types apply in-phase. During a typical flight cycle, the peak T and CF stresses might occur at different stages of the cycle [44], on the basis that there may exist a time delay for steady state temperature field to build-up compared to the increase of rpm of the engine. It is also important to note that CF stresses vary from zero to a maximum value along the length of a turbine blade, implying that a wide range of T-CF combinations occur along the component.

It can reasonably be assumed that the above trends identified for flat repeating block geometries will generally hold for highly curved systems. The latter, however, are expected to involve an additional effect in that the wall with the smallest circumference will experience higher membrane

θ −stresses under T loading (with strains being proportional to R_h/R_c – Appendix D). This will influence the trade-off between stresses at the hole rim and the internal features, depending on whether the hot temperature is applied on a convex outer surface (suction side of blade in Fig 3c) or on a concave outer surface (pressure side of blade in Fig 3c). This will be explored in more detail in a later study.

A decision on the optimal t_c/t_h ratio requires further analysis in the creep-plastic regime, in order to determine the inelastic cyclic strain range, $\Delta\varepsilon$, experienced in the vicinity of a feature and then relate this to the number of cycles for fatigue crack initiation, N_f, based on an empirical Coffin-Manson relationship [13]. An accurate evaluation of $\Delta\varepsilon$ can be performed through traditional inelastic FE cycle-by-cycle analysis [13] or by modern, intelligent methods that determine the structural cyclic state directly [53]. Simultaneously, however, the elastic stress solutions presented here can be readily used in computationally efficient Neuber type schemes (local strain approach) [13] to determine $\Delta\varepsilon$ and thus predict N_f for the critical locations of the double wall system, over a range of loading and geometric combinations. Generally, the higher the elastic stress, the higher the local strain range and the shorter the fatigue life; nevertheless, the relationship between the fictitious elastic stress and local strain range can be complex, as it is influenced by a number of inelastic material properties, including the sharp yield stress reduction of nickel alloys beyond a temperature of 800 °C [35] and the exponential increase of creep strain rate with temperature [54] in the same regime. These properties have been shown to cause a drastic increase in local strain range for a given fictitious elastic stress. This is not a concern here for the impingement hole and inner pedestal fillet which experience temperatures less than 800 °C, but it is of major concern for the outer rim of the film hole where temperatures of ~ 1000 °C are typically experienced [31, 55]; the reduction of fatigue strength at these temperatures [56] should also be considered. This strongly suggests that attention should generally be given to the performance at the outer rim of the film hole, particularly at the

concave outer surface of the blade (high pressure side) for which film hole stresses are predicted here to be high.

The optimisation of the ratio t_c/t_h should also be informed by ratchet limit state analysis. The current problem here displays some features of the classical Bree plate problem [57], where the plate can ratchet (incrementally collapse) when the T-CF loading conditions lie beyond the ratchet boundary, leading to premature failure. The Bree problem is simple (cylindrical plate with a through thickness thermal gradient that cycles with time and a non-cycling in-plane traction loading) such that the ratchet boundary can be determined analytically with ease [57, 58]. However, the actual problem here is more complex as it additionally involves two interacting plates with holes and a temperature mismatch, a temperature dependent yield strength, significant creep in the hot wall and the traction (CF loading) also cycling with time. In this case, the ratchet boundaries can be determined numerically through modern schemes, such as the Linear Matching Method [53], which uses the elastic stress field solutions into search algorithms for the residual stress field and iterative algorithms based on shakedown theorems [59]. Nevertheless, geometric and material model idealisations can be used to simultaneously obtain analytical expressions for the ratchet boundary, by using directly the analytical elastic solutions presented here within classical [60] and extended [61] shakedown theorems. Such solutions will provide physical insight into the ratchet mechanisms that occur in these new double wall systems and the sensitivity of the ratchet boundary with respect to the t_c/t_h ratio. Again, all the above highlight the utility and importance of the currently presented elastic solutions in design.

In later design stages, one needs to consider a number of geometric features in addition to the t_c/t_h ratio, including global features such as pedestal spacing, and local features such as hole shape and size. In our previous study [12] we showed that a narrower pedestal spacing decreases the SCF at holes due to hole-hole and hole-pedestal interaction effects. A further decrease can be achieved by manipulating the shape of the film hole and reducing its inclination. However, these results, together

with the new results presented here, should be interpreted with caution. Modern turbine blades consist of single crystal Nickel alloys, which display orthotropic properties [5]. Therefore, highly porous systems with more dense arrays of holes and pedestals may activate slip mechanisms along crystallographic planes of the FCC lattice, eventually degrading fatigue performance. In this regard, additional parameters of the stress field need to be considered near features, such as the critical resolved shear stress/strain [23, 25, 26, 39, 41]. However, the main implications of thermal and centrifugal loading, the role of wall thickness ratio and other structural kinematic effects reported here are not expected to change for anisotropic systems. Similarly, the directional dependence of thermal and elastic properties [62] and their dependence upon temperature [63] are not expected to alter the main phenomena and trends observed here. The study presented here builds the foundation for studying how anisotropy of thermal, elastic and inelastic properties influence the stress state and therefore integrity of the system.

7 Conclusions

We have characterised temperature and stress fields in new double wall transpiration cooled gas turbine blades, with the aim of increasing substantially the efficiency of future turbomachines. The relationship between geometry, temperature field and stress field is studied and explained and the implications for the optimal design of double walled systems is evaluated. The study demonstrates that low cycle fatigue (LCF) due to superimposed thermal (T) and centrifugal (CF) stresses at cooling holes is a major concern in these systems. Stresses due to gas pressure are found to be less important.

Our aerothermal CFD results show that the new systems experience significant temperature gradients across the hot outer-wall thickness and down the length of the pedestals. This results in a severe temperature mismatch between the walls, and as a result significant compression and tension in the hot and cool walls, respectively. These primary characteristics are found to dictate the thermal stresses. The role of second order characteristics, such as the temperature variation along the plane

of the hot wall due to coolant film superposition, is found to be less significant. Thus, it is demonstrated that using idealised temperature fields can be a useful strategy in conceptual design.

The kinematic constraints involved in the new double wall blade design imply that thermally induced stresses are strongly biaxial and change depending on whether the thermal gradient through the hot wall thickness or through the pedestal height dominates, and are sensitive to the wall thickness ratio; a thinner cool wall reduces the peak compressive stresses at the film cooling holes, but increases tensile stresses at internal features, i.e. the impingement holes and the pedestals.

These effects for pure T loading also apply when uniaxial CF stresses are superimposed; the additional effect under combined T-CF loading is an increase in tensile stresses at internal features and a reduction in the compressive film hole stress. Thus, in-phase combined loading can be beneficial to fatigue at film holes and detrimental to performance at internal features. Therefore, the optimal geometry may differ for different combinations of T-CF loading. It is demonstrated that all the above effects can be identified in a straightforward manner, through developing analytical expressions for the stress based on classical plate theory. Theoretical considerations are also found useful in providing further physical insight into the way the stress concentration factor (SCF) in the vicinity of features depends on the details of the nominal stress field.

In terms of design recommendations, film holes are suggested to be more critical for fatigue than internal features, both due to the higher stresses and to the drastic reduction of yield strength and fatigue strength of nickel alloys at high near surface temperatures (of the order of 1100 °C) experienced in practice. However, a full assessment of these structural-material effects requires solutions for the local stress-strain cyclic state in the creep-plastic regime as well as shakedown/ratchet limit solutions. Such assessments can make direct use of the elastic solutions developed here, which highlights the significance of the present study for the design of both conventional blades and the new double wall blades considered here.

Appendix A – Details of the aerothermal analysis of Section 2.1

A1. Steps 1-3

The aerothermal analysis employed to generate the results described in Section 2.1 consists of three major steps:

1. The CFD analysis (Fig 2a) only considers the internal flow of the coolant, i.e. the external flow is not simulated. It employs the following boundary conditions: hot mainstream flow temperature, T_∞, velocity, v_∞, pressure, p_∞; external heat flux, h_∞; original coolant temperature, $T_{coolant}$, and coolant mass flow rate, $\dot{m}_{coolant}$.
2. The CFD analysis provides the coolant exit velocity at the film hole, v_{film}, and thus, the blowing ratio, $\mathbb{M} = \rho_{film}\mathrm{v}_{film}/\rho_\infty \mathrm{v}_\infty$ (ρ_{film} = 12.8 kg/m^3, ρ_∞ = 7.1 kg/m^3), which are used in the empirical correlation proposed by Goldstein [46]:

$$\breve{\eta}_{f_i}(\xi,\zeta) = \frac{\mathbb{M}\mathrm{v}_{film}D_{film}}{8\,\alpha_t\left(\frac{\xi}{D_{film}} + \xi_{decay}\right)} \exp\left[\left(\frac{\zeta}{0.05\xi_{decay} + 0.6}\right)^{c_2}\right] \qquad (A1)$$

to predict the fictitious film effectiveness field, $\breve{\eta}_{f_i}(\xi,\zeta)$, along a hypothetical outer hot wall surface that contains a single film hole of diameter, D_{film}, and inclination, $\gamma = 60°$, to the surface normal, with respect to the local streamwise and spanwise positions, ξ and ζ measured from the centre of the hole (see Fig 2c). The turbulent thermal diffusivity, α_t = 146 m²/s, the function, $c_1 = 0.05\xi_{decay} + 0.6$, the constant, c_2 = 1.485, and the position, ξ_{decay} = 1.7426, at which film effectiveness becomes 0.5 along the film centreline, i.e. $\breve{\eta}_{f_i}(\xi_{decay}, 0) = 0.5$, are taken from [10], for the specific blowing ratio, $\mathbb{M}$ = 0.3, that is found to occur here for the inclination, $\gamma = 60°$. The resulting value of $\breve{\eta}_{f_i}(\xi,\zeta)$, together with the coolant temperature at the film hole exit, T_{film}, provided by CFD, are used to compute the actual film effectiveness:

$$\eta_{f_i}(\xi,\zeta) = \breve{\eta}_{f_i}(\xi,\zeta)\frac{T_\infty - T_{film}}{T_\infty - T_{coolant}} \qquad (A2)$$

for a single, independent film. This is used in the superposition relation proposed by Sellers [47] to compute the effectiveness field:

$$\eta_f(x,z) = 1 - \prod_{i=1}^{n} \Big(1 - \eta_{f,i}\,(x,z) \Big) \qquad (A3)$$

for an array of n films, with respect to the global streamwise and spanwise positions, x, z, shown in Fig 2c, where ($\eta_{f_i}(\xi,\zeta)$ in Eq (A2) is expressed as $\eta_{f,i}\,(x,z)$). The adiabatic temperature field, $\breve{T}_{max}(x,z)$, along the outer hot wall surface associated with the array of films is then determined from:

$$\eta_f(x,z) = \frac{T_\infty - \breve{T}_{max}(x,z)}{T_\infty - T_{film}} \frac{T_\infty - T_{film}}{T_\infty - T_{coolant}} \qquad (A4)$$

3. The calculated $\breve{T}_{max}(x,z)$ field for the hot outer wall surface, together with the uniform external heat flux, h_∞, are then used to determine an external heat transfer coefficient field for the entire hot outer wall surface of the array in Fig 2c. In the same manner, the CFD results of the coolant temperature field and the heat flux field throughout the internal surfaces of Fig 2a are used to determine an internal heat transfer coefficient field, which is then repeated for each unit cell of the array in Fig 2c. The internal-external heat transfer coefficient fields are used as boundary conditions in an FE convective-conductive heat transfer simulation that finally determines the steady state temperature field in Fig 2c.

A2. Details of CFD analysis

The commercial solvers ANSYS Fluent v19.1 and ANSYS mechanical were used for the CFD and FE analyses. An unstructured CFD mesh was used, with fifteen prism layers along the fluid-solid interfaces with an overall height of 0.1 mm and a growth rate of 1.2; the suitability of this mesh is based on a preliminary mesh dependence study using volume-weighted mass flow as a metric. The CFD solver is pressure-based and relies on the k-ϵ turbulence model, with an enhanced wall function

and thermal effects enabled. Air is treated as an ideal gas for the fluid domain with thermal conductivity and viscosity evaluated by the kinetic theory and the Sutherland method, respectively.

A3. Discussion on the analysis assumptions

Our film mixture calculations rely on the temperature of the coolant at the film hole exit, calculated from the CFD analysis of the internal flow. Therefore, the heat pickup in the film holes is taken into account. The fact that the CFD analysis is internal, i.e. does not account for film protection, implies that the temperature of the coolant at the film hole exit is overestimated, leading to conservative results for the film cooling effectiveness and the steady state temperature field. This suggests that, strictly, the temperature boundary conditions used in the FE thermal analysis should not be adiabatic. The same strategy has been used in [64] and is preferred here over a strategy that uses a full CFD domain for both the internal and external flow, since it provides slightly more conservative results than the actual case, in a cost-effective manner.'

Appendix B – Details of the FE analysis of Section 2.3

The ABAQUS Implicit FE scheme is used for an isotropic elastic-thermal material model with parameters taken from [63] for the CMSX-4 alloy at 700 °C in the $\langle 001 \rangle$ crystal orientation; these include Young's Modulus, $E = 100$ GPa, Poisson's ratio, $\nu = 0.4$, thermal expansion coefficient, $a = 17.4\times10^{-6}$ /°C and conductivity, $k = 19.4$ W/m°C. The mesh of Fig 2b consists of approximately 2.6×10^{5} 8-node hexahedral elements (ABAQUS code: C3D8T) and 8.5×10^{4} 4-node tetrahedral elements (C3D4T) corresponding to the film holes; 25 elements span the wall thicknesses. We consider boundary conditions consistent with our earlier studies in simpler double wall geometries [12, 34], where we showed that pedestals impose rigid kinematic coupling between the two walls, such that the thermoelastic in-plane extension of the walls must be the same and that the walls cannot rotate despite the presence of thermal gradients. These conditions are satisfied here in Fig 1b by enforcing zero z-displacements at the $\bar{z} = 0$ symmetry plane, common z −displacement for all nodes

at the $\bar{z} = 1$ symmetry plane and periodic boundary conditions at the $\bar{x} = 0$ and $\bar{x} = 1$ boundary planes. These boundary conditions and the temperature fields are respectively applied via the ABAQUS MPC and UDSIP subroutines. The periodic boundary conditions ensure that the $\bar{x} = 0$, $\bar{x} = 1$ planes in Fig 1b distort identically under thermal loading, i.e. the stress field at these planes is common. While this occurs for the idealised temperature fields (see stress contours in Figs 2f'-g'), it cannot occur for the real temperature fields used here, as these are non-periodic (Figs 2f-g). However, this does not compromise the accuracy of the solution at critical hole and pedestal locations away from the periodic planes.

Appendix C – Details of the FE turbine blade model of Section 3

The outer surface profile is produced based on x-y coordinates taken from the report by Thulin et al [1] for the root cross-section of a single wall, high pressure gas turbine blade. The internal features i.e. inner wall, spacing between the walls and inner wall ribs (see Fig 3b) are constructed in accordance with the double wall blade geometry reported by Ngetich [31]. The thickness of the walls, the ribs and the wall spacing is 1 mm; the blade is of length, $L = 60$ mm (see Fig 3b). Details of the geometry construction are available in our earlier work [34], where we used a simplified version of the blade model. The new configuration here additionally involves a cap of 1mm thickness near the blade tip (see Fig 3b), a rectangular platform (44 x 48 (mm) – see Fig 3b), an external root fillet between the outer wall the and the platform of radius $\rho_b = 3$ mm, and a fir-tree (40 mm height x 40 mm length – see Fig 3a). Inner fillets between the walls and the platform are of 0.5 mm radius. The platform, fillets and fir-tree features are used here to eliminate unphysical constraint of the walls near the blade root, particularly during thermal loading. Their exact geometry is chosen arbitrarily since the current focus is on stresses generated in the core wall regions, away from the vicinity of the blade root. The mesh consists of approximately 4×10^5 8-node hexahedral elements (ABAQUS code:

C3D8T) corresponding to the walls (with 25 elements across the wall thicknesses) and 10^5 4-node tetrahedral elements (C3D4T).

Zero y-displacements and z-displacements are prescribed on the lateral fir-tree surfaces (denoted in blue – Fig 3a) and zero x-displacement is prescribed on the front fir-tree surface (denoted in red – Fig 3a). The blue margins in Fig 3c represent the regions where the walls are coupled with pedestals according to [31]; coupling is modelled by applying a 'tie' kinematic constraint, i.e. zero relative x, y, z displacements between each node at the inner hot wall surface and its adjacent node at the inner cool wall surface. Thermal loading involves the temperatures, $T_{max} = 1038$ °C, $T_{med_h} = 940$ °C and $T_{cwall} = 778$ °C, applied uniformly along the streamwise, ξ, and spanwise, z, directions of the blade. Centrifugal loading is applied in the form of nodal forces throughout the geometry (Fig 3a); each nodal force scales with the nodal 'mass' calculated for a material density $\rho = 8.7$ tn/mm^3, the angular velocity, $\omega = 858.5$ rad/s (= 8188 rpm) and the distance of the node from the centre of the engine axis is denoted in Fig 3c; the latter is parallel to the x axis and has a distance, $R_{tip} = 400$ mm, from the xyz origin (see Fig 3b). The ω value is chosen such that a tip speed $v_{tip} = R_{tip}\,\omega = 343$ m/s (= 1 Mach); these conditions are consistent with [1] for this particular turbine blade. Loading due to rotary acceleration, $\dot{\omega}$, is also considered by using an extreme value, $\dot{\omega} = 858.5$ rad/s^2. Gas pressure distribution data are also taken from [1] to prescribe normal tractions, $p(\xi)$, on the external surface of the hot wall (indicated in Fig 3c); Fig 4a shows the $p(\xi)$ distribution, normalised over the turbine entry pressure, $p_{IN} = 1.32$ MPa; $p(\xi)$ is assumed to be constant along z.

Appendix D – Theoretical 3D solution for the cylindrical walls of Section 4.3

Kinematics

$$\kappa_{h_\theta} = \kappa_{h_z} = 0 \rightarrow \frac{M_{h_\theta}}{EI_h} - \nu\frac{M_{h_z}}{EI_h} = \frac{M_{h_z}}{EI_h} - \nu\frac{M_{h_\theta}}{EI_h} = -\frac{a\Delta T_{hwall}}{t_h} \quad (a)$$

$$\kappa_{c_\theta} = \kappa_{c_z} = 0 \rightarrow \frac{M_{c_\theta}}{EI_c} - \nu\frac{M_{c_z}}{EI_c} = \frac{M_{c_z}}{EI_c} - \nu\frac{M_{c_\theta}}{EI_c} = -\frac{a\Delta T_{hwall}}{t_c} \quad (b)$$

$$\bar{\varepsilon}_{h_z} = \bar{\varepsilon}_{c_z} \rightarrow \frac{\mathcal{N}_{h_z}}{Et_h s_h} - \nu\frac{N_{h_\theta}}{Et_h} + a(T_h - T_c) = \frac{\mathcal{N}_{c_z}}{Et_c s_c} - \nu\frac{N_{c_\theta}}{Et_c} \quad (c)$$

$$(D1)$$

$$\bar{\varepsilon}_{h_\theta} R_h = \bar{\varepsilon}_{c_\theta} R_c \rightarrow \left(\frac{N_{h_\theta}}{Et_h} - \nu\frac{\mathcal{N}_{h_z}}{Et_h s_h} + a(T_h - T_c)\right) R_h = \left(\frac{N_{c_\theta}}{Et_c} - \nu\frac{\mathcal{N}_{c_z}}{Et_c s_c}\right) R_c \quad (d)$$

Equilibrium

(forces) $N_{h_\theta} + N_{c_\theta} = 0 \quad (e)$

(forces) $\mathcal{N}_{h_z} + \mathcal{N}_{c_z} = F_{walls} + F_{ped} - F_{holes} \quad (f)$

θ, z denote bending curvature/moment and membrane strain/force components in the θ and z directions, $R_h = R - 0.5t_h$ and $R_c = R - t_h - H - 0.5t_c$ are the radii of curvature at the midplane of the hot and cool walls, respectively (see Fig 7b), whereas $s_h = R_h Z/(R - t_h)$ and $s_c = R_c Z/(R - t_h)$ are the wall arc-lengths of the unit cell in Fig 7b in the θ direction. Eqs (D1a-b) account for the fact that the total bending curvatures in each wall are zero, whereas Eq (D1d) accounts for the proportionality of wall membrane strains in the θ direction with respect to the ratio, R_h/R_c. The bending moments (and second moment of areas) and membrane forces, N_{h_θ}, N_{c_θ}, are per unit length; this is not true for $\mathcal{N}_{h_z}$, $\mathcal{N}_{c_z}$, since in the z direction we necessarily use the arc-lengths s_h, s_c to define the total wall cross-sectional area, $A_{walls} = t_h s_h + t_c s_c$, that carries the added force related to the pedestals, F_{ped}, and the deducted force, F_{holes}, related to the holes. The application of Eq (D1) for the model of Fig 1b requires replacing s_h and s_c with $4s_h$ and $4s_c$.

Appendix E – Calculation of F_{ped} and F_{holes} forces of Section 4.4

In contrast to the full population of pedestals in Fig 7a-b, the pedestals in Fig 1b are periodically absent to accommodate holes. Two planes exist where the pedestals are repeated every Z, defined in

Fig 7b, and three planes where pedestals are repeated every $2Z$. Film and impingement holes are repeated every $4Z$ in an equivalent of two planes of the unit cell (two boundary planes where the holes are cut and the middle plane where the holes are not cut - see Fig 1b). In this case, Eqs (2) lead to:

$$F_{walls} = \rho\,\omega^2 \tilde{L}_x\, 4\,(t_h s_h + t_c s_c) \qquad (a)$$

$$F_{ped} = \rho\,\omega^2 V_{ped}\left\{2\frac{L_x}{Z}\left(R_{tip} + 0.5(Z - L_x)\right) + 3\frac{L_x}{2Z}\left(R_{tip} + 0.5(2Z - L_x)\right)\right\} \quad (b) \qquad (E1)$$

$$F_{holes} = 2\rho\,\omega^2\left(V_{imp} + V_{film}\right)\left\{\frac{L_x}{4Z}\left(R_{tip} + 0.5(4Z - L_x)\right)\right\} \qquad (c)$$

where V_{film}, V_{imp} are the film and impingement hole volumes. Cutting a circular hole of diameter, D_{film}, through the hot wall at an angle, γ, to the surface normal, produces an elliptical intersection with major diameter, $\mathbb{D}_{film} = D_{film}/cos\gamma$, and a hole axial length, $\ell_{film} = t_h/cos\gamma$. This leads to $V_{film} = 0.25\pi t_h {D_{film}}^2/cos^2\gamma$ and $V_{imp} = 0.25\pi t_c {D_{imp}}^2$ (for Fig 1b $V_{imp} = V_{ped}$ since $H = t_c = D_{film} = D_{imp} = D_{ped}$ = 1mm). For $\gamma = 60°$ (Fig 1b) we get $V_{film}/V_{ped} = 4$, suggesting that the reduction of inertia in DWTC systems by the film holes is significant. Indeed, although in Figs 1a-b the pedestals are repeated 6 times more frequently than holes (the unit cell in Fig 1b contains a total of 6 pedestals and only a total of one film and one impingement hole), we obtain a ratio $F_{holes}/F_{ped} = 0.72$. As a result, the ratio $F_{ped}/F_{walls} = 0.024$ is low. For pedestals of square cross-section with $D_{ped} = 1$ mm side length, Eqs (3a-b) give $F_{ped}/F_{walls} = 0.048$ and if the height increases to the extreme value, $H = 2$ mm, the ratio becomes 0.16. These estimations indicate that the pedestals do not increase significantly the CF stresses carried by the walls.

Appendix F – Expressions for the factor $\bar{\sigma}/\sigma$ of Section 5.2

$$(\bar{\sigma}/\sigma)_{T_{max}} = \frac{0.5\left(\sigma_{T_{max\,\theta}} + \sigma_{T_{med_h\,\theta}}\right)}{\sigma_{T_{max\,\theta}}} = \frac{\bar{t}_c\left(\overline{\Delta T}_{ped} + 1\right)}{\bar{t}_c\left(\overline{\Delta T}_{ped} + 1\right) + \overline{\Delta T}_{hwall}} \qquad (a)$$

$$(\bar{\sigma}/\sigma)_{T_{med_h}} = \frac{0.5\left(\sigma_{T_{max\,\theta}} + \sigma_{T_{med_h\,\theta}}\right)}{\sigma_{T_{med_h\,\theta}}} = \frac{\bar{t}_c\left(\overline{\Delta T}_{ped} + 1\right)}{\bar{t}_c\left(\overline{\Delta T}_{ped} + 1\right) - \overline{\Delta T}_{hwall}} \qquad (b)$$

$$(F1)$$

$$(\bar{\sigma}/\sigma)_{T_{med_c}} = \frac{0.5\left(\sigma_{T_{med_{c\,Z}}} + \sigma_{T_{min_Z}}\right)}{\sigma_{T_{med_{c\,Z}}}} = \frac{2\bar{t}_h\left(\overline{\Delta T}_{ped} + 1\right)}{2\left[-\overline{\Delta T}_{cwall} + \bar{t}_h\left(\overline{\Delta T}_{ped} + 1\right)\right]} \qquad (c)$$

$$(\bar{\sigma}/\sigma)_{T_{min}} = \frac{0.5\left(\sigma_{T_{med_{c\,Z}}} + \sigma_{T_{min_Z}}\right)}{\sigma_{T_{min_Z}}} = \frac{2\bar{t}_h\left(\overline{\Delta T}_{ped} + 1\right)}{2\left[\overline{\Delta T}_{cwall} + \bar{t}_h\left(\overline{\Delta T}_{ped} + 1\right)\right]} \qquad (d)$$

In the possible range, $\infty < \bar{\sigma}/\sigma < -\infty$, we can distinguish the regimes:

- $-\infty < \bar{\sigma}/\sigma < 0$ when $\bar{\sigma} \cdot \sigma < 0$ due to the membrane force decreasing the magnitude of the in-plane stress at the surface, σ (determined from a combination of bending moment and membrane force),
- $\bar{\sigma}/\sigma = 0$ when $\bar{\sigma} = 0$ (pure bending),
- $0 < \bar{\sigma}/\sigma < 1$ when $\bar{\sigma} \cdot \sigma > 0$ and the bending moment increases the magnitude of the stress at the surface, σ (again determined by a combination of bending moment and membrane force),
- $\bar{\sigma}/\sigma = 1$ when $\bar{\sigma} = \sigma$ (zero bending),
- $1 < \bar{\sigma}/\sigma < \infty$ when $\bar{\sigma} \cdot \sigma > 0$ and the bending moment decreases the magnitude of the surface stress, σ (again from a combination of bending moment and membrane force).

Acknowledgements

The work was supported by EPSRC programme grant EP/P000878/1. Professor Peter Ireland and Dr Alex Murray are acknowledged for useful discussions.

References

1. Thulin, R.D., D.C. Howe, and I.D. Singer, *Energy efficient engine high-pressure turbine detailed design report.* 1982.

2. Murray, A.V., P.T. Ireland, and A.J. Rawlinson. *An Integrated Conjugate Computational Approach for Evaluating the Aerothermal and Thermomechanical Performance of Double-Wall Effusion Cooled Systems*. in *ASME Turbo Expo 2017: Turbomachinery Technical Conference and Exposition*. 2017. American Society of Mechanical Engineers Digital Collection.
3. Sunden, B. and G. Xie, *Gas turbine blade tip heat transfer and cooling: a literature survey.* Heat Transfer Engineering, 2010. **31**(7): p. 527-554.
4. Choi, J., et al., *Thermo-mechanical fatigue characteristics of CMSX-4 applied to the high-pressure turbine first-stage single-crystal rotor blade.* Journal of Mechanical Science and Technology, 2020. **34**(5): p. 1855-1862.
5. Reed, R.C., *The superalloys: fundamentals and applications*. 2008: Cambridge university press.
6. Broomfield, R.W., et al., *Development and turbine engine performance of three advanced rhenium containing superalloys for single crystal and directionally solidified blades and vanes.* 1998.
7. Murray, A.V., P.T. Ireland, and E. Romero, *Development of a Steady-State Experimental Facility for the Analysis of Double-Wall Effusion Cooling Geometries.* Journal of Turbomachinery, 2019. **141**(4).
8. Murray, A.V., *Advanced gas turbine cooling: double-wall turbine cooling technologies in turbine NGV/blade applications*. 2019, University of Oxford.
9. Cerminara, A., R. Deiterding, and N.D. Sandham, *Transpiration cooling using porous material for hypersonic applications.* Convective Heat Transfer in Porous Media, 2019: p. 263.
10. Murray, A.V., et al., *High Resolution Experimental and Computational Methods for Modelling Multiple Row Effusion Cooling Performance.* International Journal of Turbomachinery, Propulsion and Power, 2018. **3**(1): p. 4.
11. Krewinkel, R., *A review of gas turbine effusion cooling studies.* International Journal of Heat and Mass Transfer, 2013. **66**: p. 706-722.
12. Skamniotis, C.G. and A.C. Cocks, *Designing against severe stresses at compound cooling holes of double wall transpiration cooled engine components.* Aerospace Science and Technology, 2021: p. 106856.
13. Skamniotis, C.G. and A.C. Cocks, *Creep-plasticity-fatigue calculations in the design of porous double layers for new transpiration cooling systems.* International Journal of Fatigue, 2021: p. 106304.
14. Bunker, R.S., *A review of shaped hole turbine film-cooling technology.* J. Heat Transfer, 2005. **127**(4): p. 441-453.
15. Kim, M., et al., *Experimental investigation of effusion and transpiration air cooling for single turbine blade.* Applied Thermal Engineering, 2021. **182**: p. 116156.
16. Zamiri, A., S.J. You, and J.T. Chung, *Large eddy simulation of unsteady turbulent flow structures and film-cooling effectiveness in a laidback fan-shaped hole.* Aerospace Science and Technology, 2020: p. 105793.
17. Cerminara, A., R. Deiterding, and N. Sandham, *A mesoscopic modelling approach for direct numerical simulations of transition to turbulence in hypersonic flow with transpiration cooling.* International Journal of Heat and Fluid Flow, 2020. **86**: p. 108732.
18. Fu, W.-S., et al., *Direct numerical simulation of film cooling with a fan-shaped hole under low Reynolds number conditions.* International Journal of Heat and Mass Transfer, 2018. **123**: p. 544-560.
19. Li, W., et al., *Large eddy simulation of compound angle hole film cooling with hole length-to-diameter ratio and internal crossflow orientation effects.* International Journal of Thermal Sciences, 2017. **121**: p. 410-423.
20. Zhang, H., et al., *Effects of compound angle on film cooling effectiveness considering endwall lateral pressure gradient.* Aerospace Science and Technology, 2020: p. 105923.

21. Bashir, M.H., C.-C. Shiau, and J.-C. Han, *Film cooling effectiveness for three-row compound angle hole design on flat plate using PSP technique.* International Journal of Heat and Mass Transfer, 2017. **115**: p. 918-929.
22. Rutledge, J.L., D. Robertson, and D.G. Bogard, *Degradation of film cooling performance on a turbine vane suction side due to surface roughness.* 2006.
23. Wen, Z., et al., *A combined CP theory and TCD for predicting fatigue lifetime in single-crystal superalloy plates with film cooling holes.* International Journal of Fatigue, 2018. **111**: p. 243-255.
24. Wen, Z., et al., *Equivalent and simplification of nickel-based single crystal plates with film cooling holes.* Aerospace Science and Technology, 2018. **82**: p. 119-139.
25. Wen, Z., et al., *Prediction method for creep life of thin-wall specimen with film cooling holes in Ni-based single-crystal superalloy.* International Journal of Mechanical Sciences, 2018. **141**: p. 276-289.
26. Wang, J., et al., *The inter-hole interference on creep deformation behavior of nickel-based single crystal specimen with film-cooling holes.* International Journal of Mechanical Sciences, 2019. **163**: p. 105090.
27. Kim, K.M., et al., *Optimal design of impinging jets in an impingement/effusion cooling system.* Energy, 2014. **66**: p. 839-848.
28. Zhou, Z., et al., *Effect of skew angle of holes on the tensile behavior of a Ni-base single crystal superalloy.* Journal of Alloys and Compounds, 2015. **628**: p. 158-163.
29. Zhou, Z.-J., et al., *Effect of skew angle of holes on the thermal fatigue behavior of a Ni-based single crystal superalloy.* Acta Metallurgica Sinica (English Letters), 2017. **30**(2): p. 185-192.
30. Zhou, H., et al., *Crystal plasticity analysis of cylindrical holes and their effects on the deformation behavior of Ni-based single-crystal superalloys with different secondary orientations.* International Journal of Plasticity, 2019. **119**: p. 249-272.
31. Ngetich, G.C., et al., *A three-dimensional conjugate approach for analyzing a double-walled effusion-cooled turbine blade.* Journal of Turbomachinery, 2019. **141**(1).
32. Elmukashfi, E., et al., *Analysis of the Thermomechanical Stresses in Double-Wall Effusion Cooled Systems.* Journal of Turbomachinery, 2020. **142**(5).
33. Skamniotis, C. and A.C. Cocks, *Minimising stresses in double wall transpiration cooled components for high temperature applications.* International Journal of Mechanical Sciences, 2020. **189**: p. 105983.
34. Skamniotis, C.G. and A.C. Cocks, *2D and 3D thermoelastic phenomena in double wall transpiration cooling systems for gas turbine blades and hypersonic flight.* Aerospace Science and Technology, 2021: p. 106610.
35. Sengupta, A., et al., *Tensile behavior of a new single-crystal nickel-based superalloy (CMSX-4) at room and elevated temperatures.* Journal of materials engineering and performance, 1994. **3**(1): p. 73-81.
36. Dixon, S.L. and C. Hall, *Fluid mechanics and thermodynamics of turbomachinery*. 2013: Butterworth-Heinemann.
37. Ince, A., G. Glinka, and A. Buczynski, *Computational modeling of multiaxial elasto-plastic stress–strain response for notched components under non-proportional loading.* International Journal of Fatigue, 2014. **62**: p. 42-52.
38. Coudon, F., et al., *A stochastic approach applied to directionally solidified turbine blades.* International Journal of Solids and Structures, 2020. **184**: p. 193-201.
39. Cunha, F., M. Dahmer, and M. Chyu. *Thermal-Mechanical Life Prediction System for Anisotropic Turbine Components*. in *Turbo Expo: Power for Land, Sea, and Air*. 2005.
40. Zhang, X., et al., *Crystal orientation effect and multi-fidelity optimization of a solid single crystal superalloy turbine blade.* Computational Materials Science, 2018. **149**: p. 84-90.
41. Hou, N., et al., *The influence of crystal orientations on fatigue life of single crystal cooled turbine blade.* Materials Science and Engineering: A, 2008. **492**(1-2): p. 413-418.

42. Segersäll, M., D. Leidermark, and J.J. Moverare, *Influence of crystal orientation on the thermomechanical fatigue behaviour in a single-crystal superalloy.* Materials Science and Engineering: A, 2015. **623**: p. 68-77.
43. XiaoAn, H., et al., *Viscoplastic analysis method of an aeroengine turbine blade subjected to transient thermo-mechanical loading.* International Journal of Mechanical Sciences, 2019. **152**: p. 247-256.
44. Kauss, O., et al., *Structural analysis of gas turbine blades made of Mo-Si-B under transient thermo-mechanical loads.* Computational Materials Science, 2019. **165**: p. 129-136.
45. Kumar, R., et al., *Thermo-mechanical analysis and estimation of turbine blade tip clearance of a small gas turbine engine under transient operating conditions.* Applied Thermal Engineering, 2020. **179**: p. 115700.
46. Goldstein, R.J., *Film cooling*, in *Advances in heat transfer*. 1971, Elsevier. p. 321-379.
47. Sellers Jr, J.P., *Gaseous film cooling with multiple injection stations.* AIAA Journal, 1963. **1**(9): p. 2154-2156.
48. Ngetich, G.C., et al., *A Three-Dimensional Conjugate Approach for Analyzing a Double-Walled Effusion-Cooled Turbine Blade.* 2019. **141**(1): p. 011002.
49. Chowdhury, N.H., H. Zirakzadeh, and J.-C. Han, *A predictive model for preliminary gas turbine blade cooling analysis.* Journal of Turbomachinery, 2017. **139**(9).
50. Poursaeidi, E., et al., *Effects of natural frequencies on the failure of R1 compressor blades.* Engineering Failure Analysis, 2012. **25**: p. 304-315.
51. Maktouf, W. and K. Sai, *An investigation of premature fatigue failures of gas turbine blade.* Engineering Failure Analysis, 2015. **47**: p. 89-101.
52. Timoshenko, S.P. and J. Goodier, *Theory of elasticity.* 2011.
53. Ma, Z., et al., *A unified direct method for ratchet and fatigue analysis of structures subjected to arbitrary cyclic thermal-mechanical load histories.* International Journal of Mechanical Sciences, 2021. **194**: p. 106190.
54. Nathal, M., et al., *Stress relaxation behavior in single crystal superalloys.* Materials Science and Engineering: A, 2015. **640**: p. 295-304.
55. Ngetich, G.C., P.T. Ireland, and E. Romero. *Study of Film Cooling Effectiveness on a Double-Walled Effusion-Cooled Turbine Blade in a High-Speed Flow Using Pressure Sensitive Paint*. in *Turbo Expo: Power for Land, Sea, and Air*. 2019. American Society of Mechanical Engineers.
56. Scholz, A., et al., *Modeling of mechanical properties of alloy CMSX-4.* Materials Science and Engineering: A, 2009. **510**: p. 278-283.
57. Bree, J., *Elastic-plastic behaviour of thin tubes subjected to internal pressure and intermittent high-heat fluxes with application to fast-nuclear-reactor fuel elements.* Journal of strain analysis, 1967. **2**(3): p. 226-238.
58. Bradford, R., *The Bree problem with primary load cycling in-phase with the secondary load.* International journal of pressure vessels and piping, 2012. **99**: p. 44-50.
59. Chen, H. and A.R. Ponter, *Shakedown and limit analyses for 3-D structures using the linear matching method.* International Journal of Pressure Vessels and Piping, 2001. **78**(6): p. 443-451.
60. Adibi-Asl, R. and W. Reinhardt, *Non-cyclic shakedown/ratcheting boundary determination–Part 1: Analytical approach.* International journal of pressure vessels and piping, 2011. **88**(8-9): p. 311-320.
61. Ponter, A. and S. Karadeniz, *An extended shakedown theory for structures that suffer cyclic thermal loading, Part 2: applications.* 1985.
62. Li, Z., et al., *Deformation and recrystallization of single crystal nickel-based superalloys during investment casting.* Journal of Materials Processing Technology, 2015. **217**: p. 1-12.
63. Dye, D., et al. *Welding of Single Crystal Superalloy CMSX-4: Experiments and Modeling*. in *Superalloys 2004 (Tenth International Symposium)*. 2004.

64. Murray, A.V., P.T. Ireland, and E. Romero, *Experimental and Computational Methods for the Evaluation of Double-Wall, Effusion Cooling Systems.* Journal of Turbomachinery, 2020. **142**(11).